27th AIAA Applied Aerodynamics Conference
22 - 25 June 2009, San Antonio, Texas

AIAA 2009-3616

Conceptual Design for a Laminar Flying Wing Aircraft

T.I. Saeed* , W.R. Graham† , H. Babinsky ‡ , J.P. Eastwood § , C.A. Hall ¶ , J.P. Jarrett ‖ , M.M. Lone **and K.A. Seffen ††

Department of Engineering, University of Cambridge, Trumpington St., Cambridge, CB2 1PZ, England

Growing air travel, with its associated environmental impact, is increasingly becoming a public concern. The laminar flying wing (LFW), which utilises boundary layer suction as a means of laminar flow control, has been proposed by Greener by Design as a potential solution, with preliminary estimates suggesting a significant reduction in fuel-burn. The purpose of this study is to investigate whether a conceptual design which supports this assertion can be produced. The starting point is to find the overall size, cruise speed and cruise altitude that satisfy constraints imposed by the LFW configuration: subcritical flow, limited by Reynolds number, efficient flight and satisfactory passenger accommodation. By treating the aircraft as an unswept 'flying plank', we find that a maximum section thickness-to-chord ratio of 28%, a chord length of 8.9 m, a span of 80 m, along with a cruise Mach number of 0.58 at an altitude of 10900 m and a cruise weight of 69 tonnes, meet these demands. A planform and section geometries are then developed to allow an estimate of the suction required to maintain laminar flow; this is 20.7 kgs^{-1}, requiring 625 kW of power. The associated cruise thrust is 7.6 kN; the engine is designed to provide this plus the off-take to power the suction system and auxiliary components. The resulting specific fuel consumption is 18.4 g/kN.s. The structural weight is estimated via standard preliminary design methods for a metal aircraft, and is 30.5 tonnes. With the operating empty weight determined, and 32.2 tonnes allowed for fixments, passengers (120) and baggage, 6.3 tonnes is left available for cruise fuel; on the basis that 5.2 tonnes is usable, this gives a 4125 nm range at a fuel-burn of 6 g/pax.km. The longitudinal static stability of the design remains an issue: the estimated centre-of-gravity range implies that a feedback control system would be required.

I. Introduction

With the growing traffic in air travel, focus is being increasingly drawn to the environmental impact caused by commercial aircraft emitting combustion products into the high-level atmosphere. Whilst new aircraft continue to achieve some reductions in fuel-burn and harmful emissions, the possible improvements are constrained by the overall configuration, which to a large extent has not changed in the last 50 years. The Greener by Design group proposed, in 2001, that a 70% reduction in specific fuel-burn could be achieved with a laminar flying wing (LFW) aircraft having 2050 technology in contrast to current aircraft of 2001 technology.[2] The LFW utilises suction as a means of laminar flow control (LFC) through porous wing surfaces to maintain a laminar boundary-layer at Reynolds numbers typical of a transitional or turbulent boundary-layer, thus reducing drag. The LFW layout lends itself well to LFC as there is a much higher percentage of wetted area that can be laminarised in comparison to conventional aircraft designs where the fuselage poses a problem.[21]

The last detailed LFW conceptual design was by Handley Page in 1961.[3] The aim of this work is to carry out a new aerodynamic and engineering study of the LFW in order to assess whether the suggested

*Research Student, Fluid Mechanics, Student Member AIAA.
†Senior Lecturer in Aircraft Aerodynamics, Member AIAA.
‡Reader in Aerodynamics, Senior Member AIAA.
§Master's Student, Fluid Mechanics.
¶University Lecturer, Member AIAA.
‖University Lecturer, Member AIAA.
**Master's Student, Fluid Mechanics.
††Senior Lecturer in Structural Engineering, Member AIAA.

reduction in fuel-burn is achievable. The research looks at five key design areas: stability and control - design of planform layout and control surface geometry; wing design - optimisation of 2D sections subject to flow constraints and cabin volume requirements; boundary-layer stability - estimation of the viscous drag and suction power; propulsion system - design of an engine that maximises efficiency at cruise and is capable of providing both the required thrust and suction power; and structures and weights - initial sizing of structural elements and weight estimation. First, however, it is necessary to specify the aircraft's overall size and its cruising parameters. This is the topic of the following section.

II. Aircraft and Mission Specification

For the sake of simplicity, an unswept 'flying plank' of span b and constant chord c is considered. We investigate the dependence of weight and cruising parameters on span and thickness-to-chord ratio (t/c), subject to constraints applicable to the LFW configuration.

The principal constraint on the design of the LFW is that of maintaining a laminar boundary-layer over the maximum wetted area. It is therefore important that the aerofoil remains subcritical in order to avoid the formation of shock waves, because the associated sharp increase in pressure promotes boundary-layer transition or even separation. Hence the cruise Mach number M_{cruise} is chosen to be lower than the critical Mach number for a given wing section thickness-to-chord ratio and lift coefficient C_L.

In 1956 Pfenninger demonstrated, on an F.94 aircraft, a maximum chord-based Reynolds number, Re_c, for laminar flow stabilised by suction, of 36.4 million.[3] Due to advancements in LFC since then, a higher value could possibly be achieved. However, for the purposes of this investigation Re_c is limited to 40 million.

A minimum value of 2.5 m is imposed on the maximum wing section thickness, as a cabin height of at least 2 m must be provided for passengers to stand upright. The extra 0.5 m is to allow for the placement of pipes and pumps used to suck the air from the boundary-layer, the wing structural reinforcements and other various fittings. It is immediately apparent that having t/c comparable to current high-speed subsonic aircraft is impractical; 10%, for example, would require a chord of 25 m.

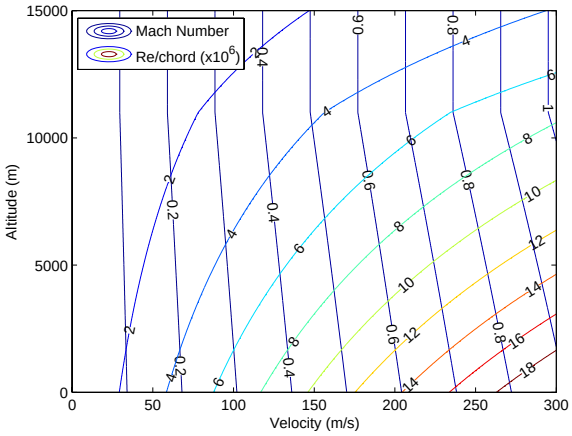

Figure 1. Altitude against velocity with contours of Mach number and Re_c/c.

Figure 1 shows how Mach number and unit Reynolds number vary with altitude for the American Standard Atmosphere.[14] Self-evidently, the Reynolds number at a given altitude can be lowered by reducing cruise speed. Less obviously, for a given cruise speed, the Reynolds number decreases with altitude, but with an associated increase in Mach number until the tropopause is reached at 11km.

For given values of t/c and M_{cruise}, Figure 1 allows us to determine cruise conditions as follows. The chord is defined by t/c and the thickness constraint (2.5 m), and the maximum allowable unit Reynolds number is then $\frac{40\times10^6}{c}$. Following this contour until $M = M_{cruise}$ sets the maximum allowable cruise speed and the corresponding altitude.

The critical Mach number, and hence M_{cruise}, depends not only on t/c, but also C_L. A first estimate of cruise C_L is obtained by assuming a drag polar of the form in Equation 1, where the first and second terms are the zero-lift and lift-dependent drag terms respectively.[18] The latter is expected to be dominated by induced drag, and is thus written as a multiple, k, of the expression for an elliptical loading distribution of aspect ratio A_R. Here, we assume $k = 1.1$. (For the flying plank, $A_R = b/c$. For a given span b, A_R increases

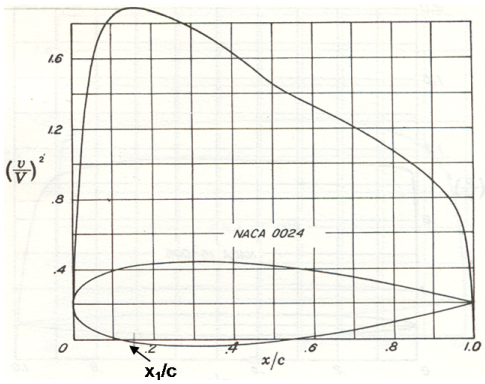

Figure 2. NACA0024 velocity profile.[7]

linearly with t/c, because of the fixed thickness constraint.)

$$C_D = C_{D0} + \frac{kC_L^2}{\pi A_R} \tag{1}$$

By differentiating Equation 1 and assuming that cruise is at maximum lift-to-drag ratio (L/D), we obtain

$$C_L = \sqrt{\frac{\pi C_{D0} A_R}{k}}. \tag{2}$$

In order to proceed further with an estimate of the dependence of C_L, and hence M_{cruise}, on t/c, it is first necessary to obtain an estimate of C_{D0}. A crude estimate of C_{D0} may be obtained from the velocity profile of a standard symmetrical aerofoil, such as that shown for a NACA0024 section in Figure 2. By assuming a linear velocity profile from the stagnation point up to the suction peak at x_1 the skin friction may be integrated using Thwaites' method.[5] Between $x_1/c < x/c < 1$, assuming suction maintains a laminar boundary-layer on the verge of transition with a constant momentum thickness, C_{D0} may be estimated using a method proposed by Eppler and Somers, which makes use of the energy and momentum integral equations.[6] The process is repeated for a range of NACA00 sections with various thickness-to-chord ratios, such that an approximate relation between C_{D0} and t/c can be derived, as detailed in Figure 3, and used in subsequent calculations. For the NACA0024 section illustrated in Figure 2, $C_{D0} = 1.027 \times 10^{-3}$.

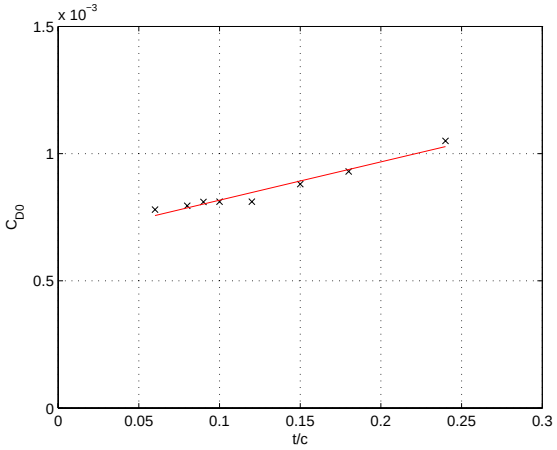

Figure 3. Varition of estimated C_{D0} with thickness-to-chord ratio.

In Figure 4 (a) the variation of C_L with t/c and b is shown. Current aircraft typically cruise at a C_L of around 0.5,[19] here it is apparent that the expected cruise C_L for the LFW is much less than this. Take for example $t/c = 0.3$ and b = 80 m, this gives $C_L = 0.17$, 66% lower than current aircraft due to the low value of C_{D0} achieved via LFC. It is interesting to note that in the Handley Page proposal, the suggested cruise C_L for the HP117 is 0.17.[3] The increase in C_L with t/c is due to the corresponding increase in aspect ratio as the chord drops; this outweighs the weak growth of C_{D0}. Increasing span at fixed t/c also increases aspect ratio, without changing C_{D0}.

Current jet aircraft typically have a cruise L/D of 15-20.[19] Here, due to the laminar boundary-layer, C_D at maximum L/D is only about 0.002 and so for $t/c = 0.3$ and b = 80 m, an L/D of around 80 is potentially achievable. The associated L/D values are plotted in Figure 4 (b). Like the lift coefficient, L/D increases with span and t/c.

An estimate of the critical Mach number, and hence M_{cruise}, is provided by applying the Prandtl-Glauert correction to a 2D panel method solution.[20] The latter provides the incompressible suction peak pressure coefficient C_{pi}^{min} for a given NACA00XX aerofoil at various lift coefficients. The corrected pressure coefficient at free-stream Mach number M_∞ is then

$$C_p^{min} = \frac{C_{pi}^{min}}{\sqrt{1 - M_\infty^2}}, \tag{3}$$

and the flow is locally sonic when

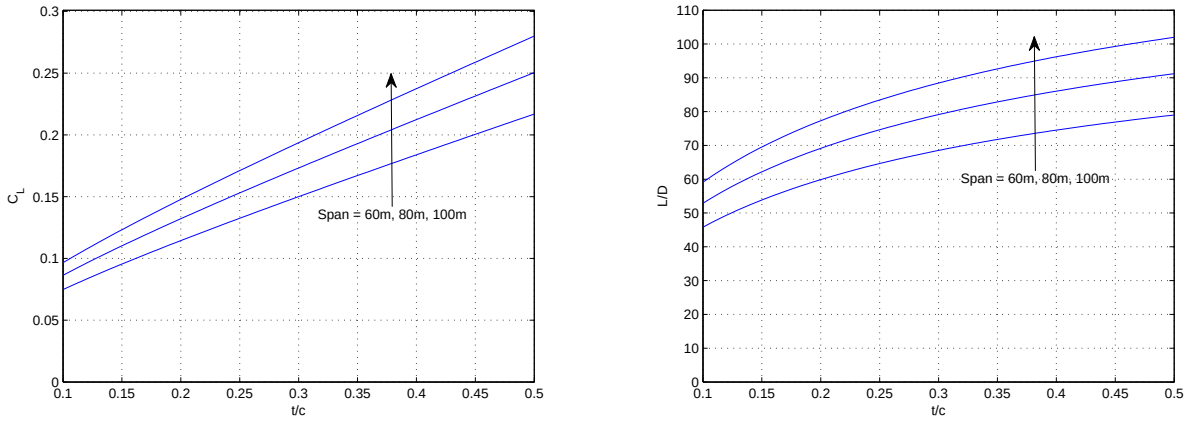

(a) (b)

Figure 4. Variation of: (a) cruise C_L and, (b) cruise L/D with t/c and span.

$$C_p^{min} = \frac{2}{\gamma M_\infty^2}\left[\left(\frac{2+(\gamma-1)\,M_\infty^2}{\gamma+1}\right)^{\frac{\gamma}{\gamma-1}} - 1\right], \tag{4}$$

where γ is the ratio of specific heats. The solution $M_\infty = M_{crit}$ to equations 3 and 4 is the critical Mach number for the aerofoil section at the given lift coefficient.

Howe[8] gives the following simple formula for M_{crit} in terms of C_L and t/c, assuming an unswept configuration:

$$M_{crit} = A_f - 0.1C_L - \left(\frac{t}{c}\right). \tag{5}$$

Here A_f is a number which depends on the standard of aerofoil section. For older aerofoils A_f is around

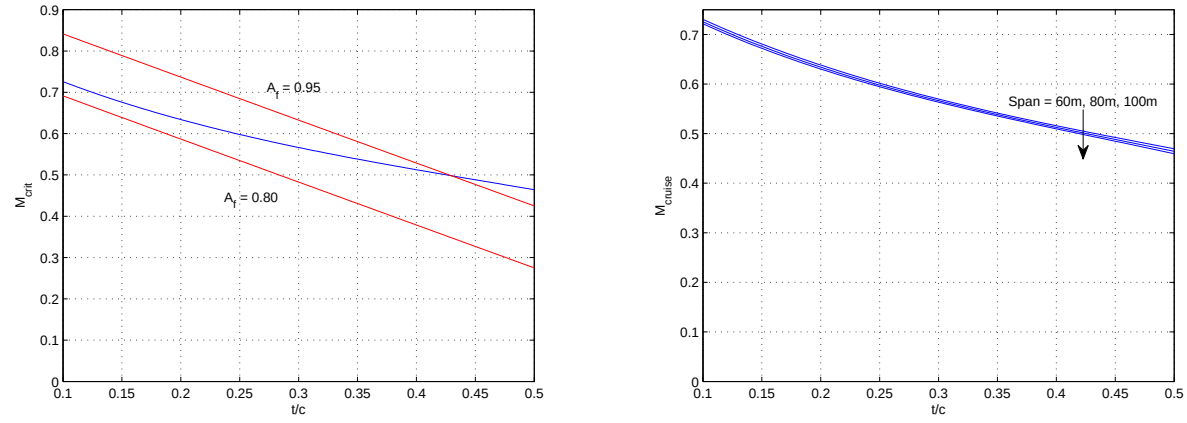

(a) (b)

Figure 5. (a) Comparison of critical Mach number; (b) calculated cruise Mach number dependence on t/c and span.

0.8 but a value of 0.95 should be possible with an optimised advanced aerofoil. Figure 5 (a) compares the variation of M_{crit} with t/c (C_L specified via Equation 2 in both cases) using our method and that provided by Howe - our estimate of M_{cruise} lies between the extremes of Equation 5 in the range $0.1 < t/c < 0.4$.

The calculated cruise Mach number is shown as a function of the thickness-to-chord ratio and span in Figure 5 (b). As expected, it reduces with increasing t/c. Span variations have little effect because M_{cruise} is insensitive to lift coefficient changes at the low values found here.

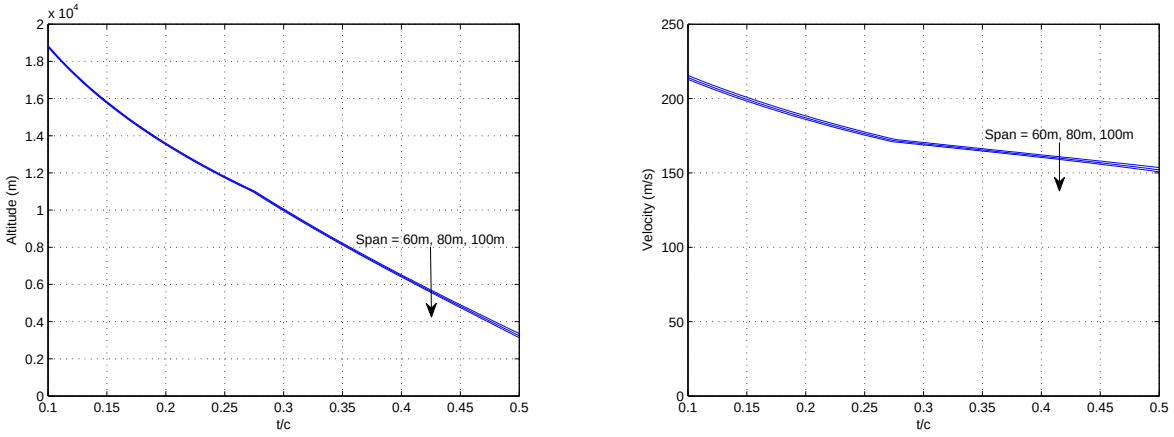

(a) (b)

Figure 6. Variation of: (a) cruise altitude and, (b) speed with t/c and span.

This completes the calculations needed to specify the cruising altitude and speed. Figure 6 details the variation of these two parameters with t/c and span. The noticeable kink here, and in subsequent plots, at about $t/c = 0.27$ is due to the tropopause at 11 km, where there is a change in the dependence of atmospheric conditions with altitude. Flight above the tropopause, in the stratosphere, has potentially greater pollution impact,[2] and places greater demands on the pressurised structure; there are also associated problems with weather patterns such as the jet stream and clear air turbulence [a]. On the other hand, flight below the tropopause implies thick aerofoil sections and low cruise speeds.

The maximum cruise weight, due to lift, is $\frac{1}{2}\rho U_\infty^2 bcC_L$, where U_∞ is the cruise velocity. Figure 7 (a) shows that cruise weight increases with t/c - cruise altitude drops and so the atmospheric density increases, as does C_L (due to the rise in aspect ratio) and these factors outweigh the decrease in $U_\infty^2 c$. Taking a span of 80m and $t/c = 0.2$ as an example, the cruise weight is about 60 tonnes - considerably less than that of the HP117, which was proposed at about 122 tonnes.[3]

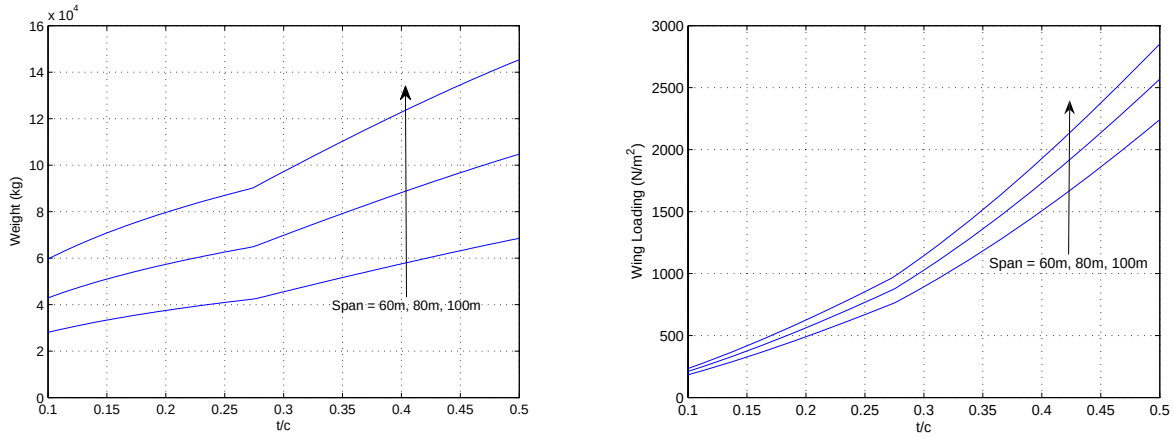

(a) (b)

Figure 7. Variation of: (a) cruise weight and, (b) wing loading with t/c and span.

The wing loading is best interpreted as the average pressure difference carried by the wing and is given by Equation 6. Figure 7 (b) shows that wing loading increases with t/c faster than weight, due to the corresponding wing area reduction. Nonetheless, the values are very low compared with conventional passenger aircraft (the Boeing 737-200 has a wing loading of 5660 Nm^{-2}),[26] raising the prospect of an unacceptably high structure weight fraction.

[a]Section A65.1, http://www.faa.gov/

$$w_L = \frac{1}{2}\rho U_\infty^2 C_L \tag{6}$$

A force balance at cruise leads to the net cruise thrust, X_N, in Equation 7. The low cruise weight and high L/D give rise to a low cruise thrust requirement. Figure 8 shows that X_N increases gradually with t/c but less quickly than W, because the increasing aspect ratio improves the lift-to-drag ratio. For comparison, a B737-600 has a cruise thrust specification of around 26.3 kN per engine [b]. However for the proposed LFW in this study, X_N is about 8 kN for a wing with span 80m and maximum thickness-to-chord of 0.28.

$$X_N = \frac{W}{L/D} \tag{7}$$

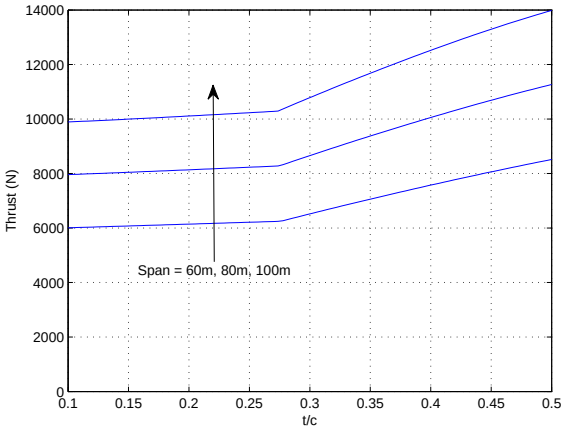

Figure 8. Variation of cruise thrust with t/c and span.

The study thus far suggests that a higher t/c is favourable because wing loading and cruise L/D increase with t/c. However the consequence of a higher t/c is an unusually low cruise velocity. Based on a compromise between these issues, and also on the desire to cruise at an altitude below the tropopause, a design t/c of 28% was selected. The benefits of increasing span will, in practice, be limited by structural issues; b was thus set at the maximum currently allowed by airports: 80 m. The design cruise altitude is 10.9 km at a cruise Mach number of 0.58 and cruise weight of 69 tonnes.

III. Stability and Control

The two main constraints affecting the design of the aircraft planform and control surfaces are the maximisation of area available for boundary-layer suction and the reduction of induced drag. AVL 3.26, a numerical design tool that implements the vortex lattice method [c] was used to estimate 3D lift distributions, induced drag and aircraft stability derivatives (and therefore modes of motion). As there are currently no specifications on flying and handling qualities related to the flying wing arrangement, U.S. military specifications [d] are used to guide the design.

The effects of wing taper were investigated for the unswept flying plank with 2 m high wingtip fins. As taper increases, the neutral point initially travels forwards, but then moves aft. The Dutch roll natural frequency and damping also decrease, due to the reduction in wingtip fin root length. Roll stability decreases due to the reduction in the moment of inertia about the longitudinal axis, improving roll performance. The lift on the outboard sections goes up, leading to potential wingtip stall issues. Finally, strong taper adversely affects induced drag. A taper ratio of 0.8 was found to give reasonable stability and lift distribution properties.

The influence of wing sweep on stability was investigated by using the same model with pure sweep and no taper. Longitudinal static stability improves as sweep is increased, because the neutral point moves aft. Although lightly damped, the Dutch roll mode is increasingly stabilised as sweep approaches approximately 35°. Further increases in sweep have a destabilising affect. However, Dutch roll natural frequency increases with sweep. The SPO damping ratio also increases but its natural frequency decreases, while the phugoid mode's damping ratio decreases. Increasing wing sweep has a similar effect to taper on the roll subsidence mode. For sweep angles less than 20°, the spiral mode was found to destabilise, but angles greater than 20° were found to have a stabilising effect on the spiral mode.

Dutch roll natural frequency is dependent on the moment the wingtip fins can exert when the aircraft is perturbed. This moment depends both on the wingtip fin height and the available moment arm - more sweep increases the moment arm, making the wingtip fins more effective. It is important that wetted area

[b] http://cobweb.ecn.purdue.edu/ propulsi/propulsion/jets/tfans.html
[c] http://web.mit.edu/drela/Public/web/avl/
[d] MIL-F-8785C and MIL-F-9490D. The LFW is put into Class III; the aim is to meet Level 1 flying qualities in flight phases B and C.

is minimised as this contributes to minimising areas requiring laminarisation and so an optimum wingtip fin height was determined as a function of sweep angle. Simulations showed that the minimum wingtip fin height to meet MIL-F-8785C specifications for Dutch roll natural frequency occurs at 40° sweep, and is just less than 4 m.

Introducing wing sweep also leads to a lift valley in the lift distribution as well as an increase in the outboard loading. Thus too much sweep can lead to a lift distribution prone to wingtip stall and with higher induced drag. Here, sweep is limited to 25°, so that attention can be restricted to Tollmein-Schlichting instabilities in the boundary-layer, rather than cross-flow disturbances.[1]

Passenger comfort when the aircraft rolls limits the distance passengers can be placed from the aircraft centreline. Assuming a tolerable vertical passenger acceleration of 0.5g at peak roll acceleration, the maximum distance for passenger seats from the centreline is 15 m. Therefore the final aircraft layout consists of a central 30 m × 8.9 m unswept section for accommodating payload; the outboard sections have a span of 25 m with a taper ratio of 0.8, sweep of 25° and 4.5 m high wingtip fins. The planform wing area is 667.5 m^2. The eventual layout has stable but lower than conventional static lateral-directional stability due to the short moment arm available to the wingtip fins, and satisfies all flight dynamics specifications except for Dutch roll damping, which must be artificially increased by a yaw damper. The aircraft's centre of gravity when fully loaded is estimated to lie 5.47 m from the leading edge [e]. With the neutral point around 15% chord forwards, at 4.8 m, the aircraft is statically unstable longitudinally. To overcome this issue, a number of options are available: a careful redistribution of applied loadings; increased sweep, though this would severely test the neglect of boundary-layer cross-flow; or 'relaxed static stability', in which the aircraft is artificially stabilised via an automated control system.

The control surfaces are designed by considering requirements for take-off and landing. Although traditionally horizontal control surfaces on a flying wing are called elevons, because they act as ailerons and elevators simultaneously, here the whole elevon is called the elevator, which acts to provide pitch control, and the outer elevons, which act differentially to provide roll authority, are called the ailerons.

The elevator design is determined by the maximum demanded pitching moment. There are two possible cases for which this demand may occur: rotation at take-off and climb-out; in this study we consider the latter. The elevators have to balance the pitching moment contributions (about the centre-of-gravity) from the engine thrust and the wing. For this calculation, the thrust line is taken half an engine diameter above the point of maximum aerofoil section height, which for a diameter of 1 m gives 1.75 m relative to the aerofoils axis of symmetry [f].

The required elevator deflection and climb-out angle of attack are found through the simultaneous solution of

$$C_{L,target} = \frac{dC_L}{d\alpha}\alpha + \frac{dC_L}{d\delta_E}\delta_E \tag{8}$$

and

$$C_{m,target} = \frac{dC_m}{d\alpha}\alpha + \frac{dC_m}{d\delta_E}\delta_E, \tag{9}$$

where the target lift coefficient, $C_{L,target}$, at a speed of 55 ms^{-1}, is around 0.55. The target pitching moment coefficient $C_{m,target}$, to balance the (nose-down) thrust contribution is 0.016 (nose-up). An elevator which comprises 90% span and 15% chord is found to give stability derivatives at climb-out of: $dC_L/d\alpha = 5.796$ rad^{-1}, $dC_L/d\delta_E = 1.466$ rad^{-1}, $dC_m/d\alpha = 0.477$ rad^{-1} and $dC_m/d\delta_E = -0.564$ rad^{-1}, from which we obtain an elevator deflection δ_E of 2.4° (downward) and climb-out angle of attack α of 4.8°. This is expected to allow enough remaining deflection for manoeuvring.

Roll control is achieved by the differential deflection of ailerons (outer elevons). The ailerons are placed as far out as possible in order to maximise the moment arm available. The design of the ailerons is based on the requirement of a 30° bank within 2.5 seconds during take-off/landing. The optimum design requires the overall elevon to be cut 12.5 m from the wingtips.

Directional (yaw) control is provided by rudders, located on the trailing edge of the vertical wingtip fins. The rudders are sized to provide sufficient yaw authority at engine out upon take-off - the engines are assumed to be separated by a distance equal to three engine diameters ie 1.5 m from the central axis, giving a yawing moment coefficient C_n of 0.00072. A 5% chord configuration requires only 6° asymmetric deflection

[e] For further details see section VII.

[f] Engine diameter calculated in section VI.

of both rudders to overcome the yawing moment. This provides enough room for manoeuvring as XFOIL viscous analysis predicts that separation over the section occurs at a deflection of 19°.

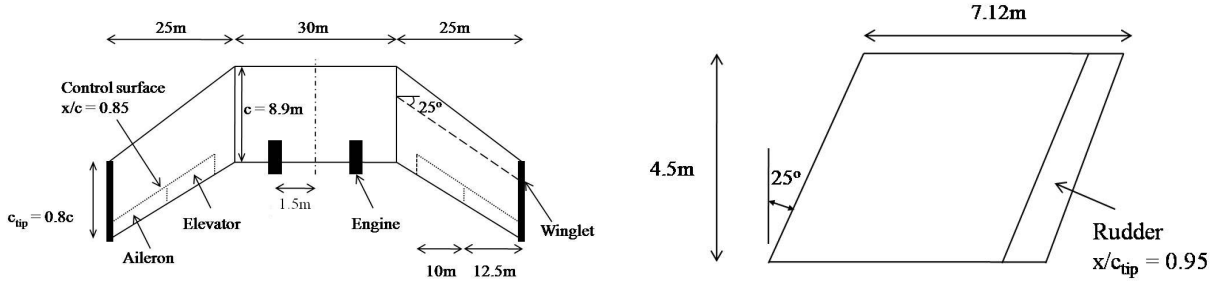

(a) Planform (b) Winglet

Figure 9. Geometric layout.

The final planform design is summarised in Figure 9. The cruise lift coefficient for this planform is $C_L = 0.18$. The resulting spanwise section C_l distribution for the LFW is detailed in Figure 10. The lift valley that arises due to sweep of the outboard section can be seen between 15-40 m; a similar effect is also noticeable out on the winglets between 40-45 m. The variation in section lift perpendicular to the leading edge, $C_{l,p}$, is superimposed on the plot, and somewhat deviates from C_l over the swept regions; it can be shown that $C_{l,p} = C_l / \cos^2 \Lambda$, assuming an infinite swept wing such that the isobars are uniform. $C_{l,p}$ is required for the boundary-layer stability calculations as this gives the resulting pressure distribution that it sees. However, for the structural loading calculations in section VII, C_l is used. In cruise, the calculated induced drag coefficient is 0.99×10^{-3} giving a k-factor (see Equation 1) of 0.92; whilst at take-off it is 0.00826.

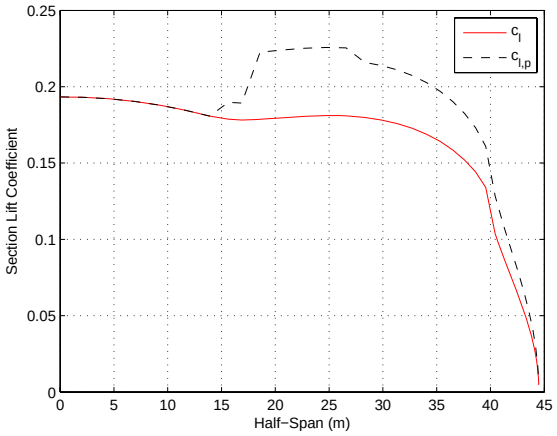

Figure 10. Section C_l along span - calculated using AVL.

IV. Wing Design

To simplify the structural design task, a 'multi-bubble' design comprising intersecting transverse cylinders was chosen for the pressurised cabin, with the number of bubbles determining the number of rows of seats. To allow for the wing's structural elements as well as the suction hardware, the diameter of each bubble is taken as 2.25 m. The bubble overlap is chosen to give a minimum cabin height of 2 m. The joint spacing is then just over 1 m, comparable with current seat pitches, so we specify one seat row per bubble. Finally, assuming an effective seat width of 1 m (i.e. 0.75 m seats, with a 0.75 m 'trolley gap' every 3 seats) gives a capacity of 120 passengers.

For the preliminary calculations, a NACA0028 section was assumed. Analysis of this aerofoil using the 2D VGK code[15] reveals that it becomes supercritical at only 0.5% above M_{cruise}, due to the significant curvature associated with such a high thickness. A more sophisticated section is clearly necessary. There are three design limitations: maintain subcritical flow, reduce adverse pressure gradient that would otherwise promote boundary-layer transition/separation, and enclose the multi-bubble pressure vessel. A bespoke aerofoil section generator was first created. The generator takes the suction surface of the leading edge of an RAE2822 supercritical section, to ensure good performance in this aerodynamically critical region, and fits a cubic Bezier curve to the remaining surface. The curve is then mirrored to form a symmetric section, and this is expanded to the required thickness. The use of a Bezier curve provides low-order parametrisation, thus aiding the efficiency of the design process; it also ensures 2^{nd} order continuity in the aerofoil surface.

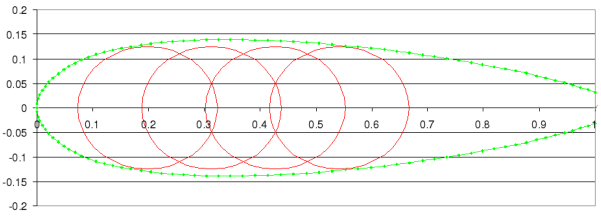

Figure 11. Inboard aerofoil section design with blunt trailing edge showing the passenger pressure vessel in red.

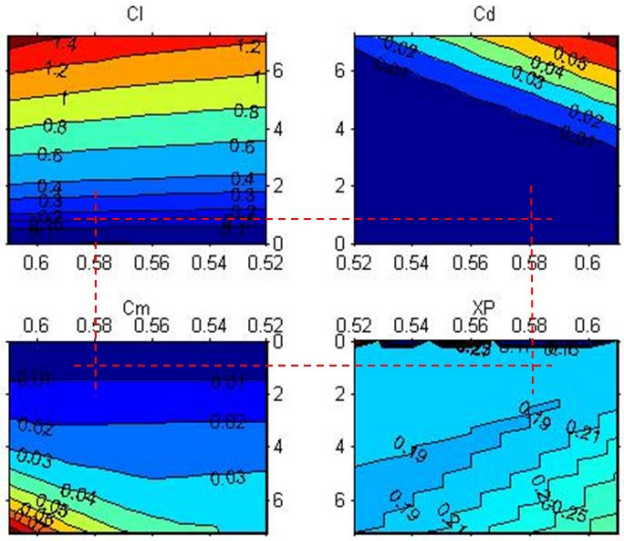

Figure 12. C_L, C_D, C_M and centre of pressure performance of the inboard aerofoil design with incidence (in degrees - vertical axes) and M_∞ (horizontal axes) around the cruise condition (the intersection of the dashed lines).

With the large internal volume and section thickness requirements, there was a tendency towards extreme trailing edge pressure gradients. To overcome this problem a blunt trailing edge was permitted. The resulting optimised section is shown, along with the pressure vessel, in Figure 11.

This section was investigated at different operating conditions in terms of lift coefficient, appearance of wave drag (ie when the section goes supercritical), pitching moment (minimised for stability), and centre of lift travel (which should be small for good aircraft stability). Figure 12 firstly shows that at the required design point the aerofoil is well clear of the point of significant wave drag increase (the drag rise boundary), and has a very low pitching moment. In addition the centre of lift (XP) is fixed at around 20% chord for a wide range of incidence and Mach number, indicating a stable design point. The plots also indicate no significant advantage in moving away from the chosen design point.

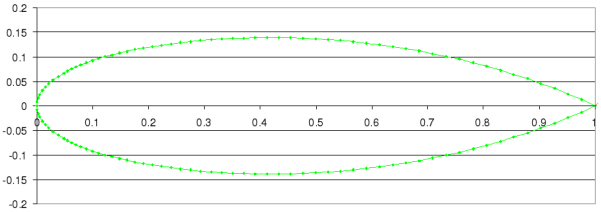

Figure 13. Outboard aerofoil section design.

The outboard section is not constrained to house a pressure vessel. However, the maximum thickness is maintained at 28% due to structural considerations, which still limits the design in terms of subcritical flow

and adverse pressure gradient trade-off. With the constraint of maintaining subcritical flow still crucial, the aerofoil section was optimised to give the highest incidence possible before supercritical flow developed. The aerofoil in Figure 13 was found to be the best in terms of subcritical range (maximum incidence of 2.75°) and adverse trailing edge pressure gradient. With a maximum thickness at a chordwise position of 42%, a favourable pressure gradient is maintained much further downstream compared to the inboard section, which will assist in reducing the amount of suction needed to maintain laminar flow.

As with the inboard section, the performance of the outboard section around the cruise condition has a clear margin before the drag rise boundary and also has good stability performance. There is no significant benefit in moving away from the cruise design condition.

V. Suction System Design

In proceeding with a suction system design, the boundary-layer stability and prediction of the required suction distribution to maintain laminar flow must first be studied; a 2D boundary-layer solver is written for this purpose. The realities of pressure losses for a given hardware design configuration and resulting power requirement are investigated. The possible blockage of surface holes due to insects, dirt or ice is neglected in this study, based on the assumption that previously suggested solutions will be effective.[1]

V.A. Boundary Layer Stability

V.A.1. The 2D Boundary Layer Solver

The Eppler method[6] is used to model the growth of the boundary-layer for a given wing surface pressure distribution, which are calculated from a set of aerofoil C_p distributions obtained using VGK.[15] For each surface panel, an initial estimate of the suction velocity normal to the surface required to avoid transition or laminar separation is found. As the initial estimate is somewhat off the minimum required to maintain the boundary-layer on the verge of transition, the calculation is iterated over each surface panel. As suction is not permissible over control surfaces, the code must also be capable of modelling a turbulent boundary-layer; again this is based on the Eppler method. For the outboard sections, an estimate of the wing viscous drag is provided by the Squire-Young method;[5] a 'far-field' approach in which the drag is obtained in subcritical (or shock-free) flows from the estimated momentum thickness of the wake far downstream of the aerofoil. This approach, however, is not applicable for the blunt trailing edge, centre-section aerofoils. Here we take the conservative approach of neglecting the above-ambient trailing edge pressure, and thus obtain the drag from the momentum deficit at that point.

The code was first validated by modelling a flow with zero adverse pressure gradient over a flat plate; the resulting boundary-layer momentum thickness profile was found to be in excellent agreement with Blasius' prediction.[5] Next, assuming a linearly retarded velocity profile, the codes ability to predict laminar separation was confirmed against Howarth's separation check.[5] The prediction of transition and separation, plus correct modelling of turbulent flow, for the flow over a range of symmetric aerofoil's and chord based Reynold's numbers, was compared against that of a known working 'in-house' code that uses Thwaites' method[5] to model a laminar boundary-layer but uses Eppler as transition and separation criteria - the viscous drag predictions (with no boundary-layer suction) were not only found to be in close agreement with this code but also with experimental results presented in Abott *et al.*[7] However, as the 'in-house' code only handles incompressible flow, a viscous calculation was also run in VGK[15] and the resulting drag estimates were in close agreement. The estimate of the degree of suction required to maintain laminar flow over a flat plate was compared against various analytical and numerical investigations performed by Head *et al.*[16]

V.A.2. Optimised Suction Estimates for the LFW

The benefits of choosing an inboard section with a blunt trailing edge over a sharp trailing edge can be clearly seen in a comparison of the two suction distributions, Figure 14. Over the rear of the latter aerofoil the suction requirements are more demanding: the total suction mass flow is 12.4 kgs^{-1} compared to 9.7 kgs^{-1} when the trailing edge is blunt.

The spanwise section C_l presented earlier in section III is used to investigate the optimised suction mass flow requirements and resulting viscous drag estimates. Figure 15 details typical suction velocity distributions for the upper surface of the inboard and outboard sections with $C_{l,p}$ values of 0.1 and 0.23 respectively. (Note

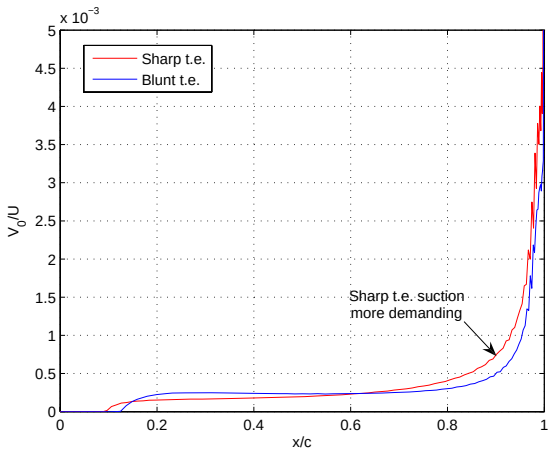

Figure 14. Distribution of suction for upper inboard section with a sharp vs. blunt trailing edge ($C_l = 0.18$).

that the Mach number normal to the swept outboard section is $M_{perp} = 0.53$.) A key feature of the plot is that suction over the first 50% of outboard chord is less demanding than inboard as its maximum thickness is further aft; after this point the outboard suction is more demanding as the aerofoil curvature, and hence adverse pressure gradient, is greater due to its sharp trailing edge compared to the inboard's blunt trailing edge. Suction is switched off outboard after 85% due to control surfaces. For comparison, work carried out on the Vampire in the mid 1950's found the maximum suction-to-flight velocity, V_0/U_∞, to be around 1.5×10^{-3}, which is of the same order of magnitude as that calculated here. The principal differences are an assumed Re_c of 20 million and a much lower section thickness in the Vampire research.[17]

With suction over all permissible areas (suction disabled at 95% and 85% chord on winglet and outboard sections respectively), the estimated mass flow that must be bled from the boundary-layer is 16.5 kgs^{-1}; whilst the viscous drag and hence zero-lift drag coefficient, C_{D0} is 0.00056. With suction switched off, the cruise viscous drag for the LFW is estimated to be 0.01. A comparison of the boundary-layer displacement thickness δ_1 for the inboard section with suction switched on and off is shown in Figure 16.

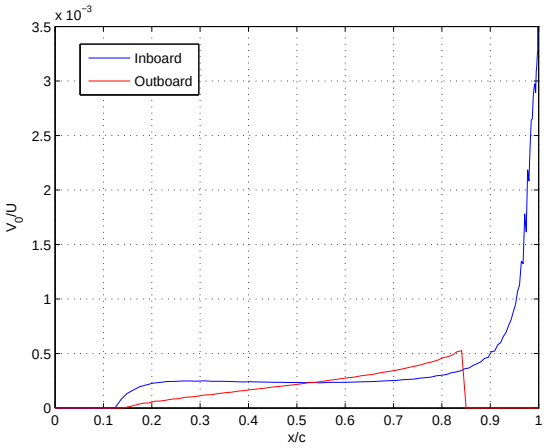

Figure 15. Comparison of inboard and outboard suction distributions, upper surface ($C_l = 0.18$).

Green[21] estimates, from suction experiments performed on the upper surface of an F-94 aircraft by Northrop, the profile drag to be 0.00018 with full chord suction, whilst for fully turbulent flow the measured profile drag is 0.00912 - 50 times greater - at a Re$_c$ of 30×10^6. Both drag predictions for the LFW are consistent with those in Green's paper; of course the wing sections are not identical but this does suggest that the predicted drags for the LFW are not unrealistic. Green proceeds to give an equivalent pump drag coefficient, which when combined with the profile drag gives the total. In this paper we calculate the pump power requirement directly.

V.B. Hardware Design

Air which is drawn through a porous surface is very nearly stagnated on exiting the small holes, and so the flow entering the suction system has a pressure equal to the local static pressure with a negligibly small dynamic pressure. As a consequence of the local pressure being generally less than ambient, suction pumps are necessary to maintain flow through the suction system. In addition, pressure losses experienced by the bled boundary-layer fluid as it passes through the suction surface and ducts have to be overcome by the

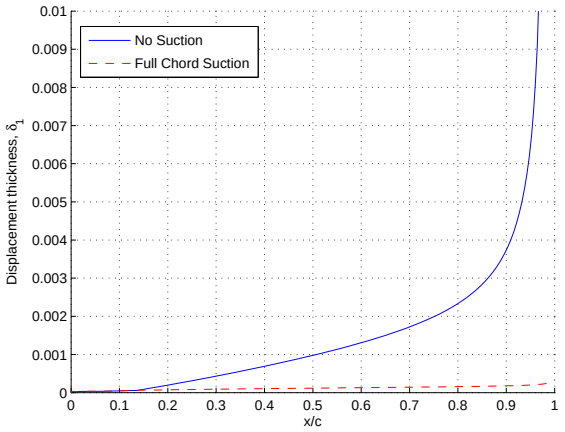

Figure 16. Comparison of the boundary-layer displacement thickness with suction on and off - upper inboard surface.

pump. The design problem is therefore to specify a surface and ducting network whose internal aerodynamics and controls allow a desired pattern of inflow to be obtained in the presence of an external static pressure distribution.[4]

The proposed suction hardware configuration is illustrated in Figure 17. The boundary-layer fluid is sucked through a porous skin and transported along spanwise chambers to a set of collector ducts. Once the flow reaches the pump, it is accelerated up to flight speed and ejected along the trailing edge of the inboard section of the aircraft.

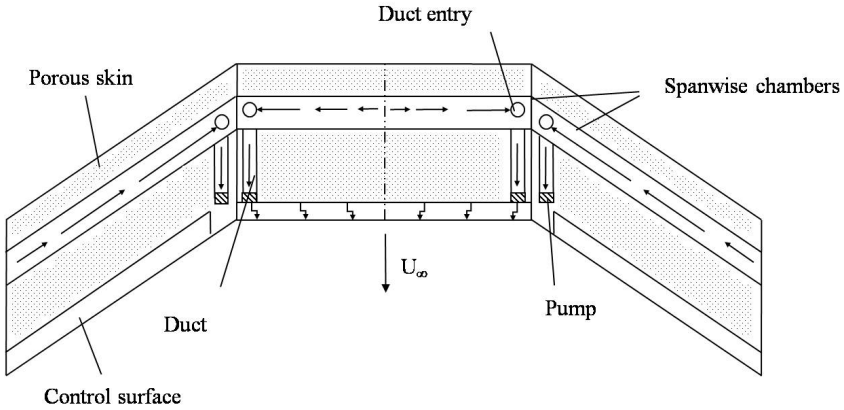

Figure 17. Suction hardware layout.

V.B.1. Overall Suction Algorithm

The algorithm structure for estimating the 'real' suction requirements for flow through the winglet and outboard sections is discussed here, as this is similar, though slightly more complicated, than the centre-section equivalent. The section lift coefficient varies with spanwise position on the wing. Although the suction requirements do become more demanding with increasing lift, the variation is small enough, at least for this investigation, to assume that the distribution of suction over the span may be taken as constant (at the highest section C_l).

- The chamber pressure is set by considering the optimised suction distribution over the outboard section and the associated pressure drop across the skin - the procedure is outlined in further detail in section V.B.2.
- The calculation then moves onto the winglets. The set outboard chamber pressures and chamber widths are mapped across to the winglet ensuring chamber section continuity between the two regions. The

optimised suction distribution for the winglet is calculated and reveals that transition occurs earlier on the winglet. An extra chamber is therefore added, with a pressure assumed equal to the chamber immediately adjacent. Due to the presence of control surfaces over the last 15% of outboard chord, arranging the chambers such that 95% of the winglet chord is laminarised is difficult; for simplicity, suction is also switched off at 85% chord on the winglets. The skin porosity distribution required to replicate the ideal suction distribution for a set pressure drop across the skin is then determined.

- As sucked fluid travels along the chamber, a pressure drop is required to overcome inertial effects associated with the injection of boundary-layer fluid and frictional losses in the conduit - see section V.B.3. It is calculated numerically, discretising the chamber in the spanwise direction. An initial estimate for the sucked mass flow over a small element is calculated using the chamber pressure set to overcome losses across the porous skin. As the chamber pressure drops, the differential pressure across the skin increases and consequently so does the suction mass flow into the chamber element. The calculation is therefore iterative and only proceeds to the next chamber element on convergence of the estimated elemental suction mass flow. The updated chamber pressure is used to begin the iteration over the next element. The laminar flow condition is continuously checked over each element.

- Once the calculation over the winglet is complete, the chamber pressures at exit from the winglet are mapped back to the outboard section - mass continuity from winglet to outboard is carefully checked. This chamber pressure is now used to determine the change in surface porosity necessary to achieve the optimised outboard suction distribution. The chamber pressure drop along the outboard section is determined in an identical manner to that discussed above. Note that the leading chamber on the outboard section is required only to transport boundary-layer fluid from the winglet to the collector duct, therefore only frictional losses are of importance.

- On reaching the inboard/outboard junction the flow travels along a chordwise collector duct and is then accelerated up to flight speed by a set of pumps and ejected out of the rear of the centre-body - discussed further in section V.B.4.

V.B.2. Initial Estimate of Chamber Pressure

To pass a certain suction mass flow across the porous skin, it is necessary to apply a pressure drop. As yet, no closed form model, independent of experimentally determined constants, has been derived that can give the required pressure difference for an arbitrary hole size at a desired hole Mach number. Here it is assumed that the porous skin has the same properties as that used in Babinsky and Galluzo's experiments (0.91 mm thick duralaminium with holes of nominal diameter 72 μm) and a curve fit to the data for a free-stream Mach number of 0.58 is used to estimate the dependence of pressure drop on suction rate.[12]

As the flow is close to stagnant on the surface of the aerofoil, the static temperature is equal to the free-stream stagnation temperature. Assuming the flow loses all the dynamic head acquired during the acceleration across the porous skin, the static temperature of the flow entering the chamber is equal to the surface static temperature, assuming the flow across the porous skin is adiabatic.[12] Provided the velocities in the chamber and ducting network are small and hence the effects of friction minimal, the static temperature throughout may be assumed constant and equal to the free-stream stagnation temperature.

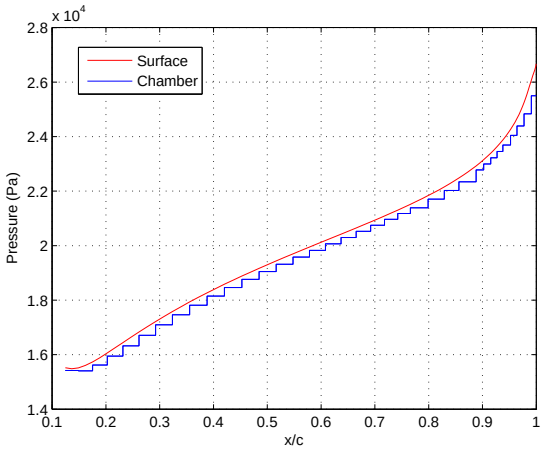

Figure 18. Chamber pressure vs. surface static pressure - upper inboard section ($C_l = 0.18$).

For a practical implementation, the optimised suction distribution is not achievable, because each chamber has a finite chordwise extent. The chamber sizes and pressures must, however, be chosen such that the variation in driving pressure differential is kept to a minimum, otherwise there would be significant variation

in the flow rate and hence wasted power. This is not the only factor driving the chamber size. As the mass flow rates increase toward the trailing edge, the chamber losses become potentially high. Setting the chamber size then becomes a compromise between increases to reduce losses, and decreases to maintain near-optimal suction. Figure 18 details an example surface static pressure and set chamber pressure. Over the first half of chord, the variation in surface pressure, and hence suction requirements, is fairly gradual, compared to the last 20%; narrowing of chamber width is evident. The differential pressure across the skin, with the chamber pressures set, is now much larger than the minimum required to achieve the optimised suction distribution. The actual hole Mach numbers must thus be checked to ensure that the holes have not become choked.

Now, with the actual velocity through the holes known, it is possible to achieve the desired suction distribution by having a variable porosity distribution - Figure 19. In practice, we use a piecewise-constant distribution. With the porosity set, the actual suction distribution that results is fed back into the boundary-layer code to confirm that laminar flow is maintained. If not, the porosity distribution is adjusted accordingly.

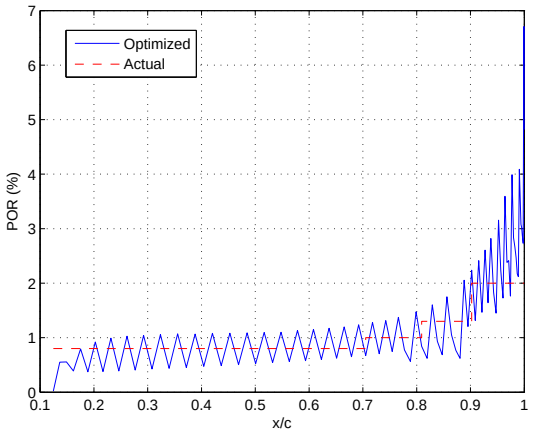

Figure 19. Porosity distribution - upper inboard section.

V.B.3. Analysis of Pressure Drop for a Tapered Chamber

The pressure drop along the chamber required to overcome frictional losses is calculated using D'Arcy's equation, along with Churchill's correlations, which model the skin friction coefficient in a pipe as a function of the flow Reynolds number; since the chambers are of rectangular cross-section, an equivalent diameter must be used.[13] The injection of boundary-layer fluid, as the flow proceeds along the chamber, also requires a difference in pressure to accelerate the flow. For incompressible flow this is straightforward to model; however compressible flow would require application of the steady flow energy equation plus other associated assumptions in addition. It is unlikely that compressibility will be an issue; the maximum total mass flow through a chamber on the upper-inboard surface is around 0.2 kgs^{-1} giving a flow Mach number of less than 0.07 for a typical chamber cross-section of 0.3 m $\times$ 0.1 m.

By application of the 1D momentum and mass continuity equations, the pressure gradient, dP/dy, over a tapered element of length δy, as illustrated in Figure 20, is:

$$\frac{dP}{dy} = \frac{\dot{m}^2}{\rho A^2}\left[\frac{1}{A}\frac{dA}{dy} - 2\frac{\dot{m}_s}{\dot{m}}\right], \tag{10}$$

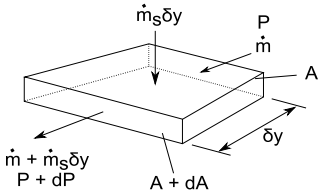

Figure 20. Notation for tapered chamber.

where A is the cross-sectional area of the element and dA/dy is the change of area due to taper; $\dot{m}$ is the mass flow entering the chamber in the spanwise direction; the flow density ρ remains constant with our assumption of incompressible flow; and $\dot{m}_s$ is the sucked mass flow per unit span. Inspection of Equation 10 reveals that, as expected, dP/dy increases with an increase in exit flow area relative to inlet, ie positive dA/dy; whilst it decreases as mass flow is added to the chamber - that is there must be a pressure drop in the flow direction if the mass flow injected is large enough.

A comparison of the static pressure drops across the skin and along the chambers of the upper-inboard section is detailed in Figure 21. It is evident that the losses along the chambers are almost insignificant to

those across the skin, as is necessary if spanwise variations in porosity are to remain small. However, both of these are fairly small in comparison to the increase in stagnation pressure difference required to discharge the suction flow at the flight speed: 5885 Pa.

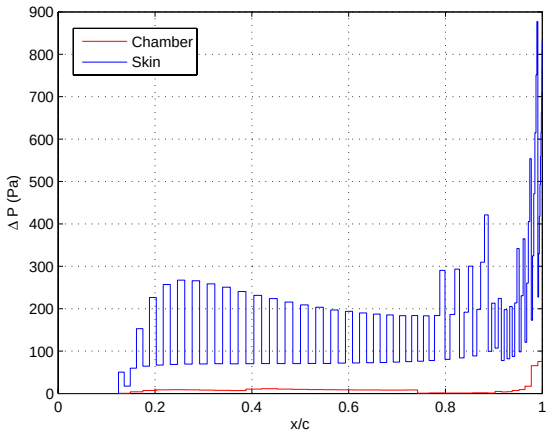

Figure 21. Static pressure drop across skin vs. along spanwise chamber - upper inboard section.

V.B.4. Ducting and Pump Arrangement

One possible solution to the design problem is to have single collector duct (per surface) that reaches a single pump, receiving sucked air from all over the wing. However, pressure recovery over the rear of the aerofoil means that the driving pressure across the skin will increase significantly making it difficult to attain the desired suction distribution. Gregory *et al*[4] proposed that the ideal solution would be to have a number of pumps, or several stages in one pump, so that the applied pressure difference can be varied over the surface of the wing, thus keeping the flow rates and losses through the skin to a minimum.

The pump power $\dot{W}_p$ for a flow with stagnation temperature T_0; mass flow at inlet to the pump $\dot{m}_{pump}$; and pump pressure ratio PPR, defined as the ratio of the stagnation pressure at exit to that at inlet, is

$$\dot{W}_p = \frac{\dot{m}_{pump} c_p T_0 \left(PPR^{\frac{\gamma-1}{\gamma}} - 1 \right)}{\eta_{pump}}; \tag{11}$$

assuming adiabatic flow and a pump efficiency η_{pump} (= 0.85 here); c_p is the specific heat capacity of air. Consideration of Equation 11 reveals that a single collector duct with a stagnation pressure equal to that of the lowest static chamber pressure and having maximum inlet mass flow for a surface will give the highest power requirement. It is therefore more efficient to have a number of collector ducts each powered by a single pump such that the stagnation pressure and mass flow can be tailored to achieve minimal power. The problem with the latter approach is that as there are quite a number of chambers, the arrangement becomes unrealistic.

The final number of ducts and pipes is decided based on a trade-off between geometric constraints (large cross-sectional areas to reduce flow velocities) and power requirements. The adopted chamber and collector duct arrangement is detailed schematically in Figure 22. As the required static pressure of adjacent chambers ($P_{c,1}$, $P_{c,2}$, $P_{c,3}$ etc) differs, flow rate devices (eg orifice plates), are needed. The lowest static chamber pressure in the series thus sets the stagnation pressure in the collector duct, $P_{0,pump}$. The mass flow entering a pump is $\dot{m}_{pump} = \dot{m}_{c,1} + \dot{m}_{c,2} + \dot{m}_{c,3} + \ldots$. The number of chambers attached to a single collector duct is limited by the overall power requirement.

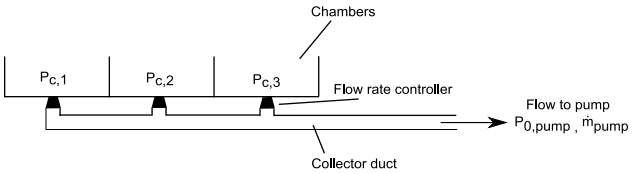

Figure 22. Duct geometry.

A trade-off study found 8 pumps per surface per side are required for the inboard section with static pressures and hence stagnation pressures, if flow velocities are negligible, as detailed in Figure 23. The mass flow at exit of a collector duct ranges between 0.25 kgs^{-1} and 0.45 kgs^{-1}. In order to keep flow velocities below around 10 ms^{-1}, and hence keep pressure drops over the ducts to a minimum, each duct should have an approximate cross-section of 0.30 m $\times$ 0.30 m. In total, the ducting for both the upper and lower surface collector ducts will occupy a width of 0.6 m and a depth of 2 m. Similar considerations for the outboard collector duct give 5 pumps per surface per side requiring a width of 0.4 m and a depth of 2 m. Therefore, 1 m span either side of the cabin is reserved for ducting.

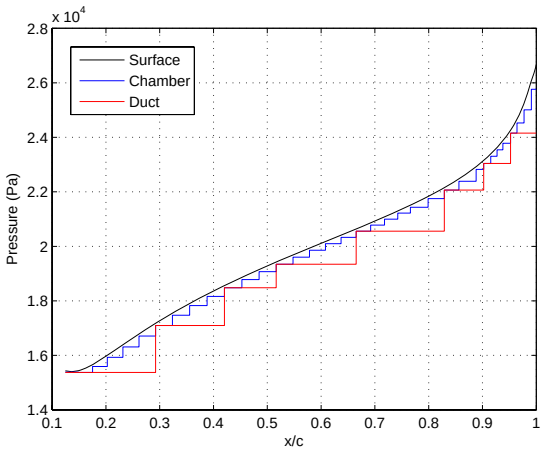

Figure 23. Comparison of surface, chamber and duct static pressures - upper inboard section.

V.C. LFW Suction Performance

The final total suction mass flow estimate is 20.7 kgs^{-1}, requiring a power of around 625 kW (if one pump per chamber were used the power would be minimised at 580 kW for this set of chamber pressures). The associated wing profile drag coefficient is calculated to be 0.00061.

Thus far only wing viscous drag has been considered. In this study, the engine nacelles are not laminarised; their drag is therefore a significant proportion of the total viscous drag. An engine dimension of 2 m diameter and 3.5 m length, which is somewhere between those for a typical current medium range aircraft and small business jet, is assumed. Nacelle drag is then estimated using methods presented in Raymer,[11] which gives $C_{D0,nacelle} = 0.0004$. This gives a total cruise C_{D0} of 0.00101. For a current long range swept wing aircraft, a typical total profile drag is 0.0180.[2] When combined with the induced drag calculated in section III, $C_D = 0.002$. For a cruise C_L of 0.18, the estimated cruise lift-to-drag ratio is 89.5 - similar to the preliminary estimates calculated in section II

The profile drag at take-off is estimated to be 0.01 (including nacelle drag); whilst the induced drag coefficient is 0.00826, assuming a take-off speed of 55 ms^{-1}; C_L is around 0.55. The resulting take-off lift-to-drag estimate is 30.1.

VI. Propulsion System

The propulsion system consists of two, two-spool, high by-pass ratio (BPR) turbofans, which must provide enough thrust at various flight conditions, in particular take-off and cruise, as well as the power necessary for suction (625 kW) and auxiliary equipment (100 kW - a default value in GasTurb [g]). The design aim is to maximise efficiency at cruise in order to minimise fuel-burn.

The required thrust at take-off mainly depends on the weight of the aircraft rather than its aerodynamic performance. With an assumed lift-to-drag ratio of 30.1 and 6° climb angle, the total required thrust is 93 kN, whilst at top-of-climb, with $L/D = 89.5$ and climb angle 0.5°, it is 14 kN. At cruise the required thrust is only 7.6 kN. The obvious design challenge here is that only around a twelfth of the take-off thrust

[g]All thermodynamic analysis and design was implemented using GasTurb - www.gasturb.de/

is needed at cruise. In addition, the engine efficiency should be highest at this flight condition to reduce fuel consumption. Therefore a relatively small engine would be preferred.

The approach to this problem is to design for the top-of-climb condition and monitor the off-design analysis performance at cruise and take-off.

At current technology levels, compressor exit temperature and turbine inlet temperature are restricted to 900K and 1800K respectively.[19] Preliminary investigations showed that these limits were most likely to be breached at the take-off condition, so top-of-climb values needed to be reduced. The fan pressure ratio (outer LPC pressure ratio) was chosen to be in the range 1.4-1.8 (typical of current engine designs); however, it was found that increasing this tended to make the engine work harder (higher non-dimensional spool speed) at take-off. A higher overall pressure ratio was found to minimise the specific fuel consumption at the design point and also helped take the cruise operating point away from the surge/stall line but at the cost of increasing the burner exit temperature T_{04} above 1800 K at take-off. Increasing the inner LPC pressure ratio at design point helped reduce T_{04} but at the expense of increasing the compressor exit temperature T_{03} above 900 K at take-off; it also helped lower the non-dimensional spool speed of the LPC at take-off. Increasing by-pass ratio helped bring down T_{04} but was limited by excessive jet velocity ratios at the design point.

The off-design HPC conditions relative to design point are detailed in Figure 24. They lie much further apart than would typically be the case for those of an engine used to power a conventional aircraft. This is primarily due to the large difference in thrust between take-off and cruise but also because of the large amount of power off-take. From Figure 24, cruise efficiency is some way off the maximum efficiency contour line - cruise efficiency was compromised to improve conditions at take-off. Most designs have the engine working hardest at the design point (top-of-climb), these results however suggest that the engine is actually working harder at take-off.

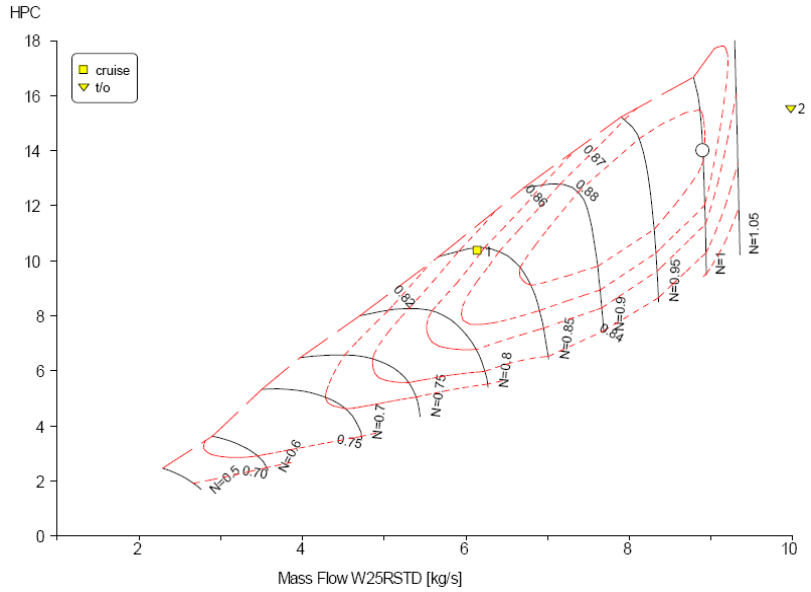

Figure 24. HPC operating map detailing top-of-climb design (circle) and off-design points - efficiency contours (red) and non-dimensional spool speed contours (black).

Table 1 shows the main parameters of the final engine design at take-off, top-of-climb and cruise. As a result of the onerous take-off condition, achieving the desired burner exit temperature and meeting the operating conditions at cruise was very difficult - the final design breaches the target burner exit temperature by 25 K. The fuel-burn is determined by the specific fuel consumption, which at 18.4 g(kN.s)$^{-1}$ in cruise, is high compared to conventional engines (note also the low overall efficiency values). This is due to the suction power requirement, and the increase is more than offset by the vastly reduced cruise drag. The resulting engine has a fan-tip diameter of 0.99 m and an estimated weight of 1000 kg (using GasTurb).

In section VII the structural weight of the aircraft is estimated; after iteration 7 tonnes remain available for fuel. To calculate the available mission fuel weight the following are considered:[24]

- Climb fuel is typically estimated as 2% maximum take-off weight (MTOW); however, taking the climb-

Table 1. Engine Design Specification.

	Take-off	Top-of-Climb	Cruise
LPC Inner Pressure Ratio	2.19	2.0	1.61
LPC Outer Pressure Ratio	1.53	1.45	1.28
By-pass Ratio	9.1	11	16.6
Net Thrust (kN)	46.5	7	3.8
Specific Fuel Consumption (g/kN.s)	10.4	15.0	18.4
Overall Pressure Ratio	33.9	28	16.7
T_{03} (K)	895	653.3	565.5
T_{04} (K)	1825	1500	1582
Propulsive Efficiency (%)	30.4	74.8	81.5
Core Efficiency (%)	45.6	43.2	32.8
Overall Efficiency (%)	13.9	32.3	26.7

out velocity of a typical jet at around 175 knots (90 ms^{-1}),[27] the fuel required to reach cruise altitude with the calculated take-off sfc and take-off L/D via the Brequet range equation[19] for the LFW is calculated at around 0.5% MTOW. A compromised value of 1% was assumed.

- Reserve fuel computed from flying 200 nm + 0.75 hrs at cruise fuel-burn rate.
- Unusable fuel estimated as 1% of the sum of climb, mission and reserve fuel.

This leaves around 5.5 tonnes available for the mission, giving a cruise range of 4125 nm. The corresponding fuel-burn is 6.0 g(passenger-kilometre)$^{-1}$. In comparison, the Boeing 777 has a fuel-burn around 23 g(passenger-kilometre)$^{-1}$.[22] The reduction is just over 70%, agreeing very well with Greener by Design's prediction.[2]

With the cruise weight at 69 tonnes, accounting for climb-out fuel etc gives an MTOW of 71 tonnes.

VII. Structures and Weight

In providing an estimate of the LFW's structural weight, it is first necessary to identify the likely critical load conditions that will dominate the design process. A first iteration considers the likely critical loads during flight, excluding self-weight as this initially unknown; however it is included in successive iterations. For comparison, the design approach adopted is also applied to an aircraft of known structural weight.

VII.A. Loading Conditions

The acceleration arising from a sharp manoeuvre is generally considered the most critical aero-load scenario for aircraft of conventional layout at around 2.5g; however, gust loads, assumed uniform across the span and acting parallel to the vertical axis of the aircraft at any instance, can sometimes reach as high as 3.5g.[11] Consider the load factor, Δn , experienced due to a vertical gust:

$$\Delta n = \frac{\Delta L}{W} = \frac{\rho V_{gust} U C_{L\alpha}}{2W/S}, \tag{12}$$

where the vertical gust velocity V_{gust} is estimated at around 11.2 ms^{-1} from statistical data presented in Raymer;[11] ΔL is the change in cruise lift; W is the cruise weight; S is the planform area; ρ is the density at cruise altitude; U is the cruise flight speed; using AVL, $C_{L\alpha}$ (the rate of change of lift with angle of attack) is 6.62 rad^{-1} for the LFW. Applying Equation 12, the resultant gust load factor is approximately 3.2g; gust loading is therefore taken as most critical.

VII.B. Design Methodology and Construction

In this study, the wing and cabin are sized in accordance with the overall design methodology detailed by Howe.[9] A safety factor of 1.5 is applied to determine the ultimate loads. The main construction material

is assumed to be Aluminium Alloy 2024-T3. There are potential advantages in using composite materials; however to exploit these would require going beyond the initial sizing calculations employed here.

VII.B.1. Cabin Structure

Cabin structures consist of three components: a skin (to resist internal pressurisation), ring frames and stringers. The internal pressurisation of the fuselage is governed by FAR codes and is set at 0.75 bar for flight altitudes above 8000 ft [h]. Both the ring frames and stringers are used to stabilise against potential local buckling and provide extra structural rigidity (eg in the event of a low speed collision). Frames also serve to transmit local shear loads to the wing structure and can be used to react pressurisation loads. Stringers may be utilised to resist some of the imposed vertical and horizontal bending moment too.

For the current aircraft, the cabin is enclosed by the unpressurised wing structure. The cabin's internal volume may be maximised by utilising a non-cylindrical configuration. To avoid significant bending loads arising due to internal pressurisation, a multi-bubble structure is opted for, as proposed by Liebeck.[25] The multi-bubble cabin structure consists of several circular cylinders combined together and joined by vertical bulkheads to make an extended structure. The vertical bulkheads have cut-outs incorporated into them to allow access between the adjoining cylinders, allowing passage throughout the cabin. Pressure bulkheads are required to cap off the spanwise extremes of the cabin from the unpressurised regions. The cabin and wing structure are assumed to be effectively decoupled for preliminary design purposes. A three-dimensional CAD model is shown in Figure 25.

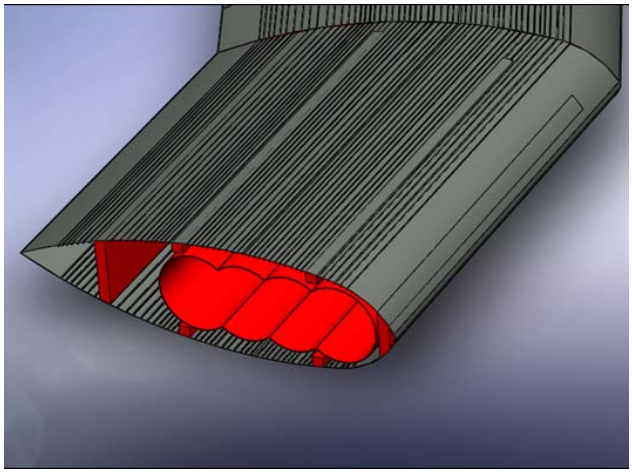

Figure 25. Section through centreboard detailing the multi-bubble structure - pressure and vertical bulkheads not shown.

With a multi-bubble configuration, the skin resists the internal pressurisation in hoop-wise tension, as long as the vertical bulkheads are placed at the 'bubble' joins. Provided the frame pitch is around 0.5 m, the allowable working stress is 100 MNm^{-1} based on crack stopping/fatigue considerations.

VII.B.2. Wing Structure

The internal wing structure consists of four main elements: the wing skin, stringers, ribs and spar-webs.

A distributed flange form of construction is used to model the wing skin, in which the upper and lower wing skins act as the main carriers of longitudinal bending moments; a proportion is also reacted by the spanwise stringers - Howe gives this split at around 65% and 35% respectively. Stringers also serve to reduce the size of areas of unsupported skin, thereby reducing local buckling loads and aiding restriction of potential deformations; finally they provide added stiffness.

A number of stringer sections are used in practice eg Zed and top hat.[9] For the LFW, the spanwise suction chambers are integrated into the distributed flange construction by allowing the top of the chamber (the wing skin) and its bottom plate to resist the bending loads, whilst the chamber walls act as stiffeners/stringers. Empirical formulae detailed in Howe give the required stringer height at around 16 times the skin thickness with an assumed pitch of 3.5 times the stringer height. There is likely to be some discrepancy between the assumed geometry and the suction calculation, in which the chambers have heights of around 10 cm over the inboard section and 20 cm over the outboard and winglet sections - their widths range between 15 cm and 30 cm. Due to the approximate nature of the structural design procedure, this detail is unlikely to be significant.

The skin-stringer panel construction depends on the bending moment at each cross-section, or rather the equivalent axial force in the top and bottom surfaces. The allowable working stress is either dictated by the buckling stability of the compression surface, assuming the properties of a light working alloy with a top hat stringer configuration, or fatigue/crack stopping requirements that result from stress fluctuations in

[h] Section 25.841, http://www.faa.gov/

the tensile surface during flight. The number of cycles the wing material must endure is 10^7, under aviation regulations, giving a stress limit of 30% of ultimate tensile strength.[28] The effective thickness of the outer skin is fixed at 1 mm (the assumed thickness of the porous material). As the wing skin and lower chamber surface are used to react bending, any remaining thickness required is provided by the latter. If the required thickness of bending material is calculated to be less than 2 mm, that of the lower surface chamber is still set to 1 mm to avoid manufacturing issues; hence there is a minimum effective wing skin thickness of 2 mm regardless of loading.

Ribs help maintain the aerodynamic shape of the wing cross-section, transmit local loads chordwise across to the spanwise beams, and help limit the length of the skin-stringer panel arrangement to an efficient column compressive strength. Pitch spacing correlations based on buckling considerations, which Howe gives to be equal to $0.55h^{\frac{1}{2}}$ [i], are used; although, in practice, rib location is also determined by layout considerations: hinge attachment points, engine and landing gear positioning etc. With the cabin enclosed by the wing, it is possible to allow the inboard wing ribs to double up as frames. Though these ribs only have a height of around 0.20 m, both on the upper and lower surfaces, full depth is used to determine their pitch, as they are linked via the cabin structure; however, if the calculated rib pitch is greater than 0.5 m (the required cabin frame pitch), then 0.5 m will be used. The depth of the outboard and winglet ribs is full section. A hybrid rib layout, whereby the ribs remain orthogonal to the front spar-web, is adopted, as this reduces structural weight.[9] This arrangement is shown schematically in Figure 26.

The spar-webs react vertical and torsional shear loads and must therefore be of sufficient depth. Consideration of the aerofoil section geometries in section IV locates the front spar at 10% chord, which allows for accommodation of the cabin in the inboard section; the rear spar is at 80%, which is as far aft as possible subject to the constraints of the control surfaces. The same non-dimensional chord positions are taken across the span, which does of course lead to a kink in the spar-web construction. A more structurally efficient layout would have a single spar-web construction running along the span. However, for a first pass at the structural weight, the difference between the two schemes is unlikely to be significant. Taking the spar heights as equal locates the shear centre at 45% chord. The allowable shear stress in the spar-webs is simply 50% of ultimate tensile stress.

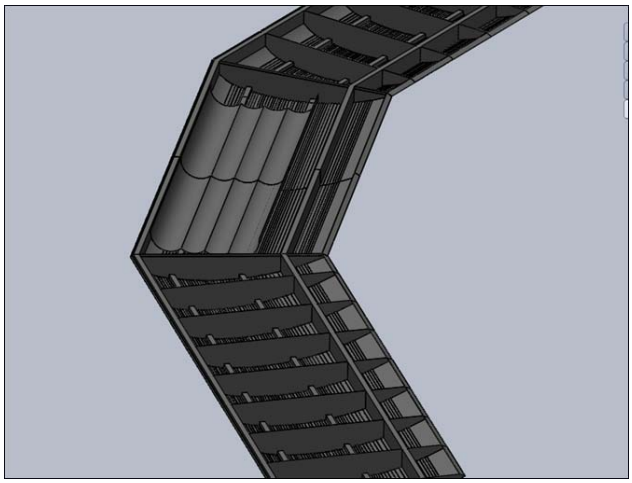

Figure 26. Plan view of wing detailing rib alignment.

VII.C. Validity of Design Methodology

To assess the validity and accuracy of the chosen design approach, an approximate analysis is performed on a Boeing 737-200; all data on this aircraft are taken from *Jane's Civil Aircraft*.[26] This aircraft cruises at an altitude of 23,500 ft with a speed of around 585 mph; the maximum take-off weight is specified at 52,500 kg and the wing planform area is 91.04 m^2; its cruise lift coefficient is therefore around 0.5. The payload specification is 15 tonnes which, based on the considerations described earlier, gives a fixment weight of 15 tonnes; the total undercarriage weight is approximately 2.1 tonnes. It is typically powered by two Pratt & Whitney JT8D turbofan engines, each weighing around 2.8 tonnes. Manoeuvre loading is taken as critical for conventional aircraft with a load factor of 2.5g.

An estimate of the structural forces (moment, shear force and torque) acting on the wing may be deduced through consideration of the likely critical loads that arise during flight; of course the prediction will be an over-estimate as self-weight would provide some bending relief (this will be considered in the analysis for the LFW). For simplicity, the aerodynamic loading is assumed elliptic with the section loading acting at quarter-chord and having zero pitching moment; the engines and undercarriage are assumed to act as point loads located on the leading edge at 35% span and the trailing edge at 2% span, respectively. The wing is treated as a root-cantilever beam with sweep neglected. Only forces at the root are used to size the wing; a

[i] 'h' is the wing depth and is measured in metres.

gross simplification that is likely to result in an over-estimate of the weight. A mean wing chord length of 3.9 m and and depth of 0.55 m are assumed. The design of the wing structural members is essentially based on the same considerations detailed in section VII.B. The width of the distributed flange is assumed to be equal to 50% of mean chord whilst the shear centre is taken at 50% chord.

The overall length of the fuselage is 31 m and the diameter is 3.5 m. As for the LFW, internal pressurisation of the fuselage is taken as the critical loading. Differences arise in the design of the cabin given that it is of a cylindrical cross-section and is not enclosed within a wing structure; as well as the stringers, the frame weight may simply be taken as 50% of the cabin skin weight.[9]

The actual wing skin weight is just over 5 tonnes whilst the fuselage weight is just under 5.4 tonnes [j]. The estimated weight of each of these items is around 6.7 tonnes (35% over) and 4.2 tonnes (25% under) respectively. Given the approximate nature of the calculated loadings, these are sufficiently close to support the structural design approach used here. Only the weights of these two items were investigated as these make up the main structures in the LFW.

VII.D. Structural Analysis and Weight

The target passenger specification is 120 persons. Each passenger is assumed to weigh 90 kg and have an associated baggage weight of 30 kg. Based on a statistical weight analysis by Hileman *et al*[24] the fixment weight is assumed equal to the total passenger weight at 14.4 tonnes; undercarriage weight is taken as 4% of MTOW (71 tonnes) giving 2.8 tonnes, and is modelled as a point load acting at 70% chord (further attention to the exact positioning is given in section VIII). Two engines, weighing 1 tonne each, are positioned at 80% chord on the inboard section at 1.5 m either side of the axis of symmetry, and treated as point loads. On the basis of correlations presented in Lachmann,[4] the combined pump and ducting weight is about 1000 kg and is 'lumped' with the engines. The fuel weight is initially unknown; it was estimated assuming a trans-Pacific range of 6000 nm at 11.5 tonnes for an initial analysis. The payload, baggage and fuel weights are assumed to be uniformly distributed between the front and rear spar-webs; the same will be true of the self-weight once it has been estimated. Around 10% of the fixment weight is made up of items such as avionics, which is modelled as a point load at the 'nose' of the aircraft whilst the remaining 90% is assumed uniformly distributed in the centrebody between the front and rear spar-webs.[24]

VII.D.1. Cabin Sizing

Subject to the pressurisation requirements discussed in section VII.B.1, the resultant cabin skin thickness for a cylinder diameter of 2.25 m is 1.8 mm. The remaining cabin components are sized as follows:

- A suggested rule of thumb proposed by Howe[9] is to take stringer mass equal to 50% of the cabin skin mass.
- Vertical bulkheads react the forces at the multi-bubble joins as illustrated in Figure 27. Force equilibrium gives $F \simeq 0.9T$, implying that the required thickness is roughly equal to that of the cabin skin. Cut-outs are neglected.
- Pressure bulkheads cap off the spanwise extremes of the cabin from the unpressurised regions. For a cylindrical pressure vessel with a semi-hemispherical cap, the stress in the cap is half the hoop-wise stress. Cap thickness is simply taken as half the cabin skin thickness. Of course such a discontinuity in thickness would induce local bending moments, and a transition would be required. For simplicity, four semi-hemispherical caps are assumed on either side, which leads to a compensating over-estimate of the actual surface area.
- The floor is designed to support the passenger and fixment loads with the frames/ribs serving as intermediate simple supports. The floor width and length are constrained by the required cabin plan area whilst the thickness is sized to react the maximum bending load.

The total cabin weight is 4795 kg; a full breakdown is given in table 2.

[j] http://adg.stanford.edu/aa241/AircraftDesign.html

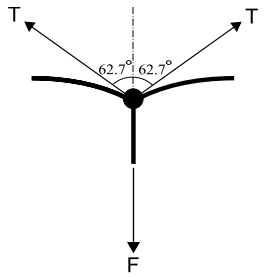

Figure 27. Vertical bulkhead force.

VII.D.2. Wing Sizing

Several of the wing sizing calculations require the local bending moment experienced by the wing. There are two loading situations that must be considered: in flight - when aerodynamic loads are present as well as self-weight plus engine and undercarriage weight; and, on the ground - when only self-weight and imposed loads (payload, baggage and fuel weight) are considered. To obtain a first estimate of the size of the main elements, the bending moment, shear force and torque distributions are evaluated through treating the wing as a root-cantilever beam as detailed in Figure 28, along with various imposed loadings.

To achieve longitudinal static stability, the neutral point must lie aft of the C.G. With the neutral point at around 4.8 m it is likely that fuel and baggage, which are located outboard, will need to be positioned as far inboard as possible. The minimum fuel tank and baggage compartment volumes may be deduced via the following considerations:

- international airliners typically limit the outside linear baggage dimensions to 200 cm, which roughly translates to a volume of around 0.3 m^3 per bag; a likely total baggage volume requirement of 55 m^3 (a factor of 1.5 has been applied to the total number of passengers). This gives an effective density of 65 kgm^{-3}; low enough to be confident in the capacity estimate;
- jet fuel has a density of around 750 kgm^{-3}; translating to a required fuel tank volume of 15 m^3 [k].

If fuel and baggage are to be placed close to inboard, taking an approximate chord length of 8.7 m and height of 1.8 m gives a minimum half-span of 0.95 m and 1.8 m respectively; recall that 1 m either side of the cabin is reserved for suction ducting.

To calculate the bending and torsion couples, the structure may be treated as an isolated member with a spanwise reference axis fixed along the locus of the shear centre of the wing box. The reference axes have an inclination of $\Lambda = 25°$ relative to the horizontal [l]. Sweeping the outboard and winglet sections gives rise to sweep discontinuities, across which the moment and torque couples must be carefully resolved. Consideration of Figure 29 reveals that the resolved moment and torque components, M^r_{i+1} and T^r_{i+1}, respectively, acting on the shaded element are given by

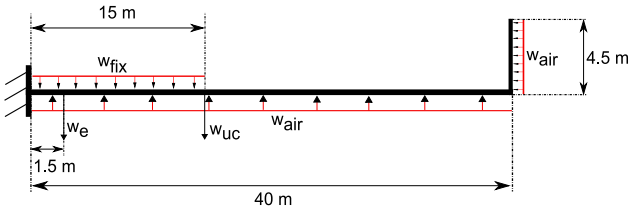

Figure 28. In-flight loading conditions - w_e, engine point load; w_{air}, distributed aero-loading; w_{uc}, undercarriage point load; and w_{fix}, distributed fixment weight.

$$M^r_{i+1} = M_{i+1}\cos\Lambda + T_{i+1}\sin\Lambda, \tag{13}$$

and

$$T^r_{i+1} = M_{i+1}\sin\Lambda + T_{i+1}\cos\Lambda. \tag{14}$$

The actual moment at 'i' is the sum of the resolved component plus the additional moment that arises due to forces acting over the shaded region, $M_i = M^r_{i+1} + \ldots$. As a result, the inboard couples are slightly over-estimated. Since the error is a conservative one, further refinement is not attempted.

[k] www.bp.com - Air BP, handbook of products

[l] Spanwise sweep at various chordwise position is taken as constant for simplicity, even though there will be slight differences arising due to taper.

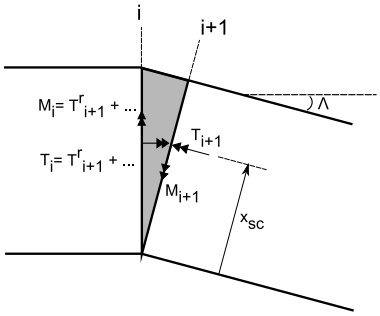

Figure 29. Resolution of forces across the sweep discontinuity.

The design is simplified by breaking down the wing structure into three regions, with the section height and chord length held constant in each: inboard and outboard - chord is 8.9 m and depth is 2.25; winglet - chord is 7.12 m and depth is 0.85 m. Only the forces at: $y = 0^+$ m, $y = 15^+$ m and $y = 40^+$ m are used for the design stage[m]. These assumptions are likely to result in an over-estimate of the wing structural weight.

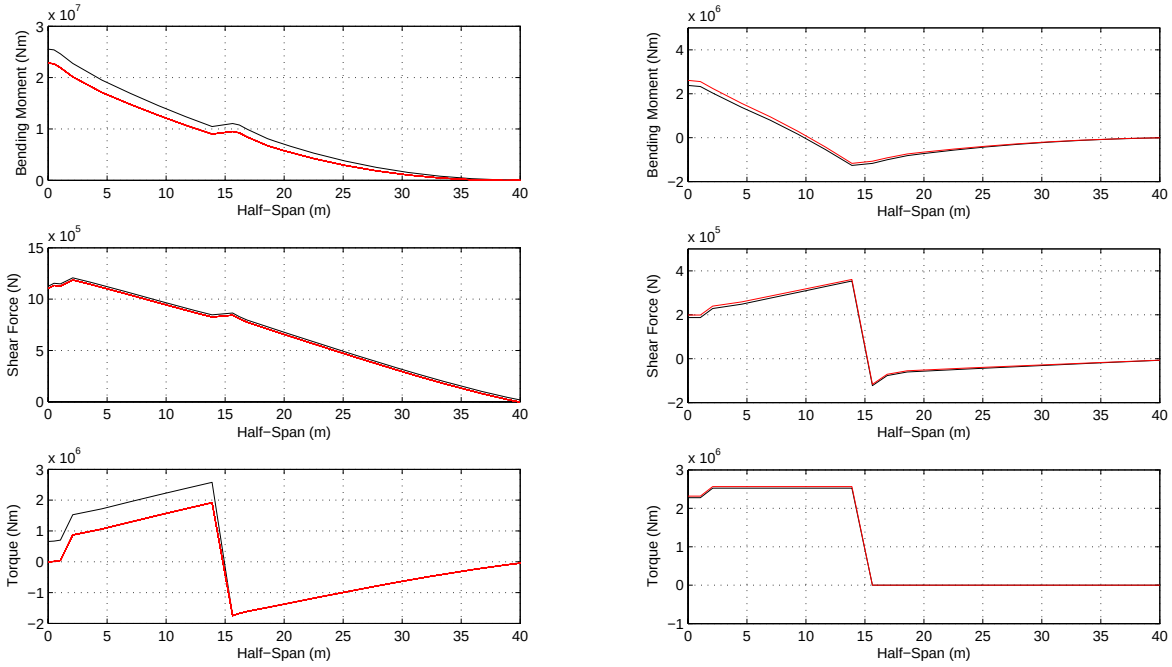

(a) In-flight (b) Ground

Figure 30. Bending moment, shear force and torque diagrams for most critical possible loading cases; initial estimate (black), final estimate (red).

The structural forces that arise when self-weight is excluded, as this is initially unknown, are shown in black in Figure 30 (a). Overall, across the span, the shear force increases going inboards. There are two distinct drops in shear force at around 15 m and 2 m. The first is due to the undercarriage and the second is due to the engine weight. The overall increase in bending moment and slight kinks in the diagram may be attributed to the same factors as those for the shear force; however, a slight reduction in bending moment also arised from the resolution of forces across the sweep discontinuity. The torque distribution shows that from 40 m to just over 15 m there is an increase in torque magnitude; at the sweep discontinuity there is a positive increase in torque, which is due to the resolved moment component. This is physically consistent; the wing is swept back, hence the overall lift on the outboard section lies aft of the shear centre of the

[m] '+' denotes force on the side of the section being considered.

inboard section. In contrast, the local lift acts forward of the shear centre of the outboard wing.

With this first calculation of the wing structural loadings, the total wing weight estimate is found to be 28470 kg and is split: 55% skin, 26% stringers, 4% shear-webs and 15% ribs.

Next, the ground loading forces must be investigated; the structure must be capable of supporting its own weight. The main ground loadings are illustrated in Figure 31 - self-weight is not shown, but is assumed uniformly distributed over the centre and outboard sections, whilst the winglet mass is treated as a point load at the tip. Note that self-weight plays no part in the evaluation of the structural forces acting on the winglet. Also, locally, the self-weight C.G coincides with the shear centre and therefore does not contribute to torque directly; however it does on resolution of forces across the sweep discontinuity.

The bending moment diagram, Figure 30 (b), reveals hogging on the outboard section; sagging occurs at the kink through the action of the reaction force via the undercarriage. There is no torque over the outboard span as the payload, baggage, fuel and structural weight's C.G are taken to coincide with the wing shear centre. A positive torque arises across the sweep discontinuity and is mainly due to the eccentricity of the reaction force, this is somewhat reduced however by the action of the self-weight over the outboard section. On comparing the in-flight and ground loading cases, the torque arising from the latter on the centre section is more critical. Re-assessing the shear-web design gives a revised wing weight estimate of 28670 kg, an increase of 200 kg.

The in-flight loading calculation, with self-weight included, is repeated, and compared against the ground loading situation once again. This process is repeated until the structural weight estimate converges. The force diagrams based on the final weight are plotted in red in Figure 30. Self-weight provides some bending relief, but does not affect the torque on the outboard section due to the coincidence of its centre of mass and shear centre. The final wing weight estimate is 25740 kg. Notice that the change in self-weight between the initial and final estimates has less of an effect on the ground loading; in-flight is more pronounced due to the 3.2g vertical acceleration.

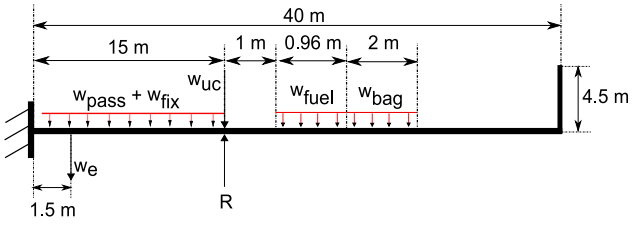

Figure 31. Ground loading - in addition to those defined in Figure 28: w_{fuel}, distributed fuel weight; w_{bag}, distributed baggage weight; w_{pass}, distributed passenger weight; and R is a point load reaction force.

The resulting structural weight breakdown is detailed in table 2.

Table 2. Structural weight breakdown.

	Wing		Cabin
Skin (kg)	13300	Skin(kg)	1980
Stringers (kg)	6300	Stringers (kg)	990
Shear webs (kg)	1490	Pressure bulkheads (kg)	70
Ribs (kg)	4660	Cabin floor (kg)	865
-	-	Vertical bulkheads (kg)	890
Total (kg)	25740	Total (kg)	4795

With this structural weight, the gross weight is 75 tonnes (4 tonnes above the allowable). Weight can either be reduced by lowering the specified number of passengers or quantity of fuel carried. The passenger specification is typical of current medium-range airliners. At the current specification, the range would be over 6000 nm; given the flight speed of the aircraft, this is somewhat large and so the fuel weight is reduced to 7 tonnes, at the sacrifice of range. Note that structural weight remains unchanged, as the most critical in-flight loading case is without payload/baggage and fuel weight.

The resulting MTOW breakdown is shown in Figure 32 and compared against that for the blended-wing Silent Aircraft.[24]

VIII. Centre of Gravity Build Up and Landing Gear Arrangement

Until now the undercarriage location has rather arbitrarily been assumed at 70% chord. The aim of this section, with the structural weight determined, is to assess how the C.G travels as various loads are applied;

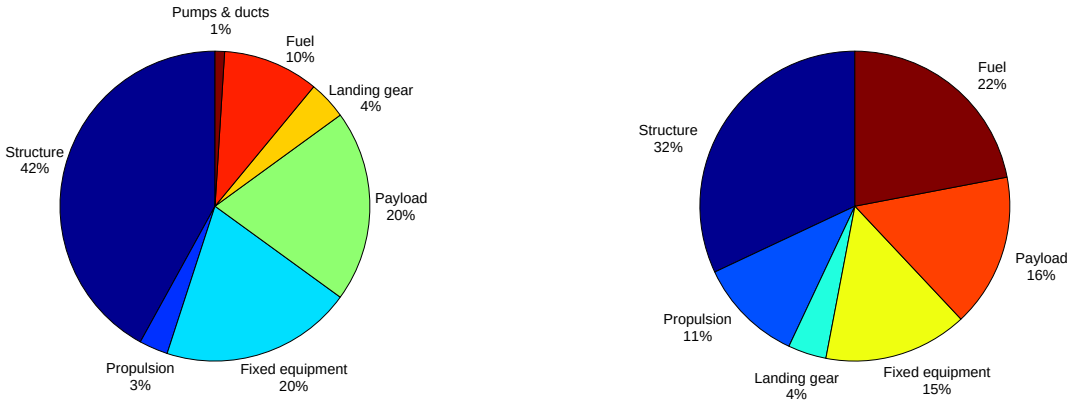

(a) LFW

(b) Silent Aircraft

Figure 32. Comparison of MTOW breakdown for the LFW against the Silent Aircraft.

hence to fix the nose and main landing gear positions.

VIII.A. Centre of Gravity Build Up

With zero payload and fuel an aircraft is at its operating empty weight (OEW). Fuel and payload can then be added in a variety of combinations and the C.G will change accordingly. The dependence of C.G location on payload and fuel mass for the LFW is illustrated in Figure 33 (a). As payload (and baggage) weight increases the C.G travels further forward; surprisingly this trend is also seen with an increase in fuel weight. Further studies, presented in Figure 33 (b), revealed that had the width of the fuel tank spanned greater than around 2 m then increasing the fuel mass would have actually shifted the C.G further aft.

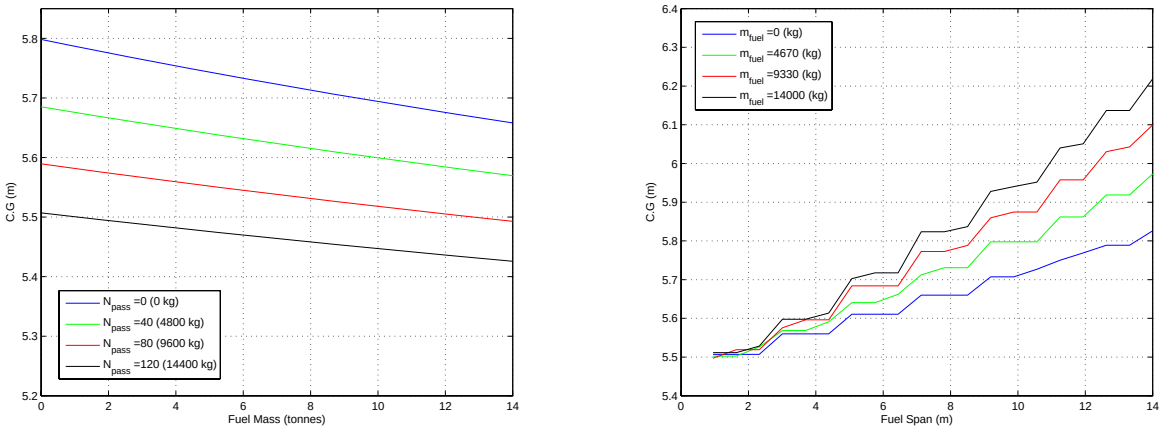

(a) Dependence on payload/baggage and fuel weight

(b) Dependence on fuel span and fuel weight for fixed payload (120 pax)

Figure 33. C.G Travel.

The extremes of C.G travel reveal that: the maximum aft position is at around 5.8 m and occurs when the aircraft is at OEW (adding baggage, in a similar manner to an increase in fuel weight, tends to shift the C.G further forwards); whilst the maximum forward position occurs when the aircraft is fully loaded and is around 5.5 m.

VIII.B. Landing Gear

One of the most common landing gear arrangements used for aircraft is the tricycle gear. Advantages include the provision of good steering after touch down and increased aircraft stability whilst on the ground.[11] The key geometric parameters of such a gear are shown in Figure 34.

With the centre of gravity located, a number of important stability criteria, whilst the aircraft is on the ground, must be adhered to. The first concerns the location of the main landing gear and hence the elevation of the aircraft; that is how high the centre of gravity is above ground level, and the need to avoid wingtip contact with the ground during take-off or landing. The maximum rearwards C.G position of 5.82 m means that the main landing gear must lie aft of this otherwise the aircraft would tip over when stationary. To prevent tip-over on take-off, the angle between the main gear, C.G and the vertical, β should be at least 15°. The length of the aircraft, measured from the leading edge to the winglet tip is 20.6 m. With a climb-out angle of attack of 4.8° (section III), a maximum take-off rotation of 10° (at which the tips touch the ground) was assumed.[11] This puts the height of the C.G above ground level, h_{cg}, at about 2.57 m, and so the gear is 0.7 m behind the furthest aft C.G position.

A second requirement concerns the nose wheel. It must not bear more than 20% of the aircraft weight; whilst if it is less than 5% then there would not be enough wheel traction for taxiing. Vertical and moment equilibrium about the leading edge gives the proportion of weight, k_{nose}, reacted by the nose wheel:

$$k_{nose} = 1 - \frac{d_{C.G}}{d_{base}}. \tag{15}$$

For k_{nose} to be reasonably small $d_{C.G}$ needs to be around the same size as d_{base} ie C.G close to the main landing gear. With the nose wheel at the leading edge, the proportion of the weight reacted when the C.G is at its forward and aft position is 15.4% and 10.8% respectively.

Finally, when taxiing around a sharp corner the aircraft must not overturn. The overturn angle ζ as illustrated in Figure 34, is the angle from the C.G to the main wheel, seen from the rear at a location where the main wheel is aligned with the nose wheel[11] - various authors give a range between 50-60°, below which an aircraft has a reduced tendency to overturn. There is no danger of the LFW overturning with a wheel track d_{track} of 30 m - at the two extremes of C.G ζ lies between 25-27°.

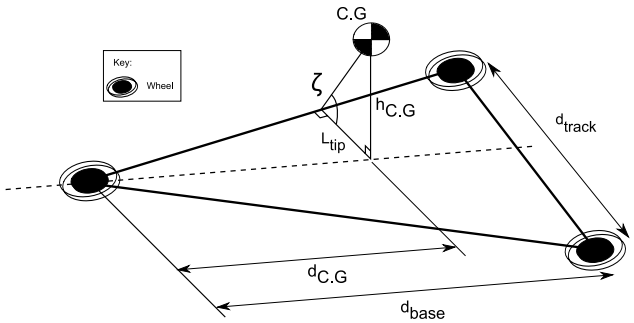

Figure 34. Overturn geometry.

IX. Conclusions

This paper has described work to date on the conceptual design of an 80m span, 69 tonne LFW, capable of carrying 120 passengers. We have estimated that, subject to the constraint of a low cruise Mach number (0.58), LFC has the potential to reduce aircraft fuel-burn by just over 70%, to about 6 g per passenger kilometre, whilst having a trans-Atlantic range of 4125 nm. The key elements of the design are:

- a 667.5 m^2 planform, of mean chord 8.3 m, with unswept centrebody and 25° sweep outer sections;
- 28% aerofoil sections, optimised to maintain subcritical flow and (in the centerbody) enclose a pressurised cabin;
- a distributed suction system capable of maintaining laminar flow over 84% of the wetted area;

- two two-spool turbofans (by-pass ratio 11) capable of providing a total thrust of 93 kN at take-off and 7.6 kN at cruise, the latter in conjunction with 725 kW of shaft power;
- a multi-bubble pressure vessel enclosed by a conventional wing structure, weighing approximately 30 tonnes.

The main design issues that arose from the study were:

- due to the constraints on sweep posed by boundary-layer stability issues, the neutral point lies aft of the LFW's centre of gravity resulting in a longitudinally statically unstable aircraft, necessitating the assumption of relaxed static stability;
- when designing the propulsion system for top-of-climb conditions, the engine was actually found to be working harder at take-off due to the large difference in thrust and power off-take between the two conditions;
- with a thrust at top-of-climb much less than conventional aircraft, the fan-tip diameter and hence weight of the propulsion system is less than 40% of a typical engine used on a medium-range aircraft; however, a high by-pass ratio is needed to meet the take-off condition making the core size relatively small;
- although the fuel weight is a smaller proportion of MTOW than is typical, with the LFW having a much lower wing loading than conventional aircraft, the structural weight takes up a much bigger percentage of MTOW and hence leaves less available weight for cargo and passengers.

Acknowledgments

The authors thank I. Vigrass and C. Ni for their initial studies on the structural weight estimation and propulsion design, respectively - carried out as part of their MEng research projects at the Department of Engineering, University of Cambridge.

References

[1]R. D. Joslin, *Aircraft Laminar Flow Control*, Annu. Rev. Fluid Mech. 1998. 30: 1-29.
[2]Greener by Design, *Air Travel, Greener by Design: The Technology Challenge*, 2001.
[3]G.V. Lachmann, *Laminarised All-Wing Aircraft - The HP117 Proposal*, 1961.
[4]G.V. Lachmann, *Boundary Layer and Flow Control*, Volume 2, Pergamon Press, 1961.
[5]A.D. Young, *Boundary Layers*, AIAA Education Series, 1989.
[6]R. Eppler & D.M. Somers, *A computer program for the design and analysis of low-speed airfoils*, NASA TM-80210, 1980.
[7]I.H. Abbott & A. E. Von Doenhoff, *Theory of wing sections*, Dover Publications Inc., 1959.
[8]D. Howe, *Aircraft Conceptual Design Synthesis*, Professional Engineering Publishing Ltd., 2000.
[9]D. Howe, *Aircraft Loading and Structural Layout*, Professional Engineering Publishing Ltd., 2004.
[10]M.C. Niu, *Airframe Structural Design*, Conmilit Press Ltd., 1990.
[11]D.P. Raymer, *Aircraft Design: A Conceptual Approach*, AIAA Education Series, 1999.
[12]P.M. Galluzo, *Fluid Dynamics of Porous Surfaces*, University of Cambridge, Engineering Department - M.Eng Report, 2000.
[13]E.S. Menon, *Piping Calculations Manual*, McGraw Hill, 2004.
[14]U.S Standard Atmosphere, NASA TM-X-74335, 1976.
[15]P.R. Ashill, R.F. Wood & D.J. Weeks, *An improved, semi-inverse version of the viscous Garabedian and Korn method (VGK)*, Tech. Rep. 87002, Royal Aircraft Establishment, BVGK, 1987.
[16]M.R. Head, *The Boundary Layer with Distributed Suction*, A.R.C. Tech. Rep., R. & M. No. 2783, 1955.
[17]M.R. Head & D. Johnson, *Flight Experiments on Boundary-Layer Control for Low drag*, A.R.C. Tech. Rep., R. & M. No. 3025, 1957.
[18]J. Katz & A. Plotkin, *Low-Speed Aerodynamics*, Cambridge University Press, 2nd Edition, 2001.
[19]N.A. Cumpsty, *Jet Propulsion*, Cambridge University Press, 1997.
[20]H. Glauert, *The Elements of Aerofoil and Airscrew Theory*, Cambridge, 1947.
[21]J.E. Green, *Laminar Flow Control - Back to the Future*, 38th Fluid Dynamics Conference and Exhibit, AIAA 2008-3738.
[22]R. Martinez-Val, E. Perez, P. Alfaro & J. Perez, *Conceptual Design of a Medium Size Flying Wing*, Proc. IMechE Vol. 221 Part G: J. Aerospace Engineering.
[23]B. Mazelsky, *Charts of Airplane Acceleration Ratio for Gusts of Arbitrary Shape*, NACA Technical Note 2036, 1950.

[24]J.I. Hileman, Z.S. Spakovsky, M. Drela & M.A. Sargeant, *Airframe Design for "Silent Aircraft"*, 45th AIAA Aerospace Sciences Meeting and Exhibit, AIAA 2007-453.
[25]R.H. Liebeck, *Design of the Blended Wing Body Subsonic Transport*, Journal of Aircraft, 41, 10-25, 2004.
[26]*Jane's Civil Aircraft*, Glasgow: Harper Collins Publishers, 30-31, 1996.
[27]H.C. Smith, *The Illustrated Guide to Aerodynamics*, McGraw-Hill Professional, 1992.
[28]M. Ashby, H. Shercliff & D. Cebon, *Materials*, Butterworth, Hienemann.